



# A Multi-instrument and Multi-wavelength High Angular Resolution Study of MWC 614: Quantum Heated Particles Inside the Disk Cavity\*

Jacques Kluska<sup>1</sup> , Stefan Kraus<sup>1</sup> , Claire L. Davies<sup>1</sup> , Tim Harries<sup>1</sup> , Matthew Willson<sup>1</sup>, John D. Monnier<sup>2</sup> , Alicia Aarnio<sup>3</sup> , Fabien Baron<sup>4</sup> , Rafael Millan-Gabel<sup>5,6</sup> , Theo Ten Brummelaar<sup>7</sup> , Xiao Che<sup>2</sup>, Sasha Hinkley<sup>1</sup> ,

Thomas Preibisch<sup>8</sup>, Judit Sturmman<sup>7</sup>, Laszlo Sturmman<sup>7</sup>, and Yamina Touhami<sup>9</sup>

<sup>1</sup> Astrophysics Group, School of Physics, University of Exeter, Stocker Road, Exeter, EX4 4QL, UK; [jkluska@astro.ex.ac.uk](mailto:jkluska@astro.ex.ac.uk)

<sup>2</sup> Department of Astronomy, University of Michigan, 1085 S. University Avenue, Ann Arbor, MI 48109, USA

<sup>3</sup> University of Colorado, Boulder, 3665 Discovery Drive, Boulder, CO 80303 USA

<sup>4</sup> Department of Physics and Astronomy, Georgia State University, Atlanta, GA, USA

<sup>5</sup> Infrared Processing and Analysis Center, California Institute of Technology, 1200 E California Blvd, Pasadena, CA, 91125, USA

<sup>6</sup> NASA Exoplanet Science Institute, California Institute of Technology, 770 S. Wilson Avenue, Pasadena, CA, 91125, USA

<sup>7</sup> The CHARA Array of Georgia State University, Mount Wilson Observatory, Mount Wilson, CA 91203, USA

<sup>8</sup> Universitäts-Sternwarte München, Ludwig-Maximilians-Universität, Scheinerstr. 1, D-81679, München, Germany

<sup>9</sup> Center for High Angular Resolution Astronomy, Department of Physics and Astronomy, Georgia State University, P. O. Box 4106, Atlanta, GA 30302-4106, USA

Received 2017 September 29; revised 2018 January 18; accepted 2018 January 31; published 2018 March 6

## Abstract

High angular resolution observations of young stellar objects are required to study the inner astronomical units of protoplanetary disks in which the majority of planets form. As they evolve, gaps open up in the inner disk regions and the disks are fully dispersed within  $\sim 10$  Myr. MWC 614 is a pretransitional object with a  $\sim 10$  au radius gap. We present a set of high angular resolution observations of this object including SPHERE/ZIMPOL polarimetric and coronagraphic images in the visible, Keck/NIRC2 near-infrared (NIR) aperture masking observations, and Very Large Telescope Interferometer (AMBER, MIDI, and PIONIER) and Center for High Angular Resolution Astronomy (CLASSIC and CLIMB) long-baseline interferometry at infrared wavelengths. We find that all the observations are compatible with an inclined disk ( $i \sim 55^\circ$  at a position angle of  $\sim 20^\circ$ – $30^\circ$ ). The mid-infrared data set confirms that the disk inner rim is at  $12.3 \pm 0.4$  au from the central star. We determined an upper mass limit of  $0.34 M_\odot$  for a companion inside the cavity. Within the cavity, the NIR emission, usually associated with the dust sublimation region, is unusually extended ( $\sim 10$  au, 30 times larger than the theoretical sublimation radius) and indicates a high dust temperature ( $T \sim 1800$  K). As a possible result of companion-induced dust segregation, quantum heated dust grains could explain the extended NIR emission with this high temperature. Our observations confirm the peculiar state of this object where the inner disk has already been accreted onto the star, exposing small particles inside the cavity to direct stellar radiation.

**Key words:** stars: individual (MWC 614) – stars: pre-main sequence – stars: variables: T Tauri, Herbig Ae/Be – techniques: high angular resolution – techniques: interferometric – techniques: polarimetric

## 1. Introduction

The key to understanding the observed diversity of planetary systems is hidden in the initial conditions of their formation, which are inherently linked to the physical conditions at play in protoplanetary disks. These disks have been extensively studied around the low-mass T Tauri stars using photometry, leading to the classification of objects from full, gas-rich protoplanetary disks to cold debris disks that exhibit only large dust grains and in some cases show evidence for an already formed planetary system (Lada 1987; Andre & Montmerle 1994). Between these two evolutionary stages, the primordial disk has  $\sim 10$  million years to form giant planets before its gas is dispersed (e.g., Sicilia-Aguilar et al. 2006), even though this timescale is debated (Pfalzner et al. 2014). Full disks are characterized by their strong infrared (IR) and millimeter emission, far in excess of what would be expected from pure photospheric emission. However, some objects display a lack of emission in the near and mid-infrared (NIR and MIR)

compared to full disk systems’ spectral energy distributions (SEDs; e.g., Calvet et al. 2005). These objects have a disk with a large dust-depleted inner cavity that has been spatially resolved with sub-mm interferometry for individual objects (e.g., Andrews et al. 2011; van der Marel et al. 2013, 2016; Canovas et al. 2015; Pinilla et al. 2015, 2017; Dong et al. 2017; Sheehan & Eisner 2017) and are called transition disks because they are believed to undergo the process of disk clearing. Between the full disk and the transitional disk stage, pretransitional objects show a depletion in the MIR but still have an excess of NIR emission, likely caused by the presence of an inner disk interior to the cavity, forming a gapped disk (e.g., Espaillat et al. 2014; Kraus et al. 2017).

For intermediate-mass, Herbig Ae/Be stars, another classification has been suggested where “Group I” objects have a positive MIR slope with wavelengths (or they can be fitted with a  $\sim 200$  K blackbody function) and “Group II” objects have a negative MIR slope (Meeus et al. 2001). Meeus et al. (2001) interpreted the Group I/II classification as an evolutionary sequence, where Group I objects represent flared disks that evolve into geometrically flat disks with a Group II-like SED. Alternatively, Maaskant et al. (2013) proposed another scheme, where a primordial flared disk evolves into either A (Group I) or B (Group II). Accordingly, in this scheme, Group I disks

\* Based on observations made with the Keck observatory (NASA program ID N104N2) and with ESO telescopes at the Paranal Observatory (ESO program IDs 073.C-0720, 077.C-0226, 077.C-0521, 083.C-0984, 087.C-0498(A), 190.C-0963, 095.C-0883) and with the Center for High Angular Resolution Astronomy observatory.

feature extended gaps, similar to the (pre-)transitional discs. However it is not clear whether the lack of IR emission indicates density-depleted gaps caused by planets (Crida et al. 2006; Papaloizou et al. 2007), photo-evaporation (e.g., Hollenbach et al. 1994), a self-shadowed region (Dullemond & Dominik 2004; Dong 2015), or the dead zone inside the disk (Pinilla et al. 2016). In some cases, the disk gap is also only partially cleared. For instance, the gap around the Herbig Ae star V1247 Orionis contains a considerable amount of optically thin dust grains that still dominate the MIR emission (Kraus et al. 2013, 2017).

The photo-evaporation mechanism can explain transition disks with small cavities and low accretion rates (Owen et al. 2011). However, transition disks with large holes and high accretion rates cannot be explained by photo-evaporation alone, and planets inside the cavity are potential candidates to sustain the accretion up to the star (Pinilla et al. 2012; Zhu et al. 2012; Owen 2014). Interestingly, these planets can also create a pressure bump at the outer disk inner edge where the largest grains ( $\sim 1$  mm) are confined, while the small grains ( $\lesssim 1 \mu\text{m}$ ) can pass through and continue to accrete toward the star. Looking for companions in the disk while the disk is in a dispersal process is therefore important to constrain these theories.

Another feature displayed by gapped disks is a high ionization degree of polycyclic aromatic hydrocarbons (PAHs) (Maaskant et al. 2014). PAHs, and more generally all quantum heated particles (QHPs), can be quantum heated when directly exposed to the ultraviolet (UV) flux from the central star (Purcell 1976; Draine & Li 2001). As such, they can reach a temperature that is higher than the equilibrium temperature at a certain radius from the star. Recently, Klarmann et al. (2017) found that an extended flux seen by long-baseline interferometry in the NIR can be explained by QHPs localized in the disk gap and demonstrated this by reproducing the NIR interferometric observations for HD 100453.

To extend our knowledge of the evolutionary phases of transition disks, we need to focus on some peculiar objects that have just started to clear the inner parts of their disk. MWC 614 (alias HD 179218) is suggested to be one such object. It is a Herbig Ae star with  $100 L_{\odot}$  (Menu et al. 2015) and whose SED was classified as Group I, consistent with either a flared or a gapped disk. Throughout this paper we use the *Gaia* distance of  $293_{-27}^{+34}$  pc (Lindegren et al. 2016). The disk was spatially resolved by NIR interferometry showing very extended emission ( $>3.1$  au; Monnier et al. 2006) and is the most resolved object in the survey of 51 Herbig AeBe stars observed by the Very Large Telescope Interferometer (VLTI)/PIONIER (Lazareff et al. 2017). The emitting material is much more extended than the theoretical dust sublimation radius predicted for a star with MWC 614's luminosity, a dust sublimation temperature of 1500 K, and a grain absorption efficiency ( $Q_{\text{abs}}$ ) of unity ( $\sim 0.35$  au; Monnier & Millan-Gabet 2002). Emission from the dust sublimation radius has been found to dominate the emission at these wavelengths for other Herbig objects (e.g., Monnier et al. 2005). Fedele et al. (2008) studied the MWC 614 disk structure in the MIR continuum using MIR interferometry with the MIDI instrument on four baselines. They deduced that the dust is mainly located in an outer disk (starting at 14.5 au) and also in a marginally resolved region ( $<3.2$  au). However, the baselines of these observations do not cover the lower spatial frequencies that set the global size and

orientation of the object. Fedele et al. (2008) interpreted the lack of emission between the two regions as being due to either a gap or a shadow cast by a puffed-up inner disk.

CO emission ( $^{12}\text{CO}$  and  $^{13}\text{CO}$  isotopologues) near  $4.7 \mu\text{m}$  has been observed in the spectrum of MWC 614 (Banzatti & Pontoppidan 2015; van der Plas et al. 2015). Similar features have been observed in the spectra of the known gapped disk systems HD 97048, HD 100546, and V1247 Orionis (Kraus et al. 2013; van der Plas et al. 2015) and are thought to arise due to the direct illumination of gas by UV stellar photons (Thi et al. 2013). This suggests that the usual sheltering provided by dust grains is absent in certain regions of the disk. Thus the existence of these lines in the IR spectrum of MWC 614 supports the idea that the disk around MWC 614 features a gap or gaps. No companion has been detected so far to explain this structure.

In this paper we describe our multiwavelength and multi-technique observational campaign to constrain the inner regions of MWC 614 (Section 2). We present the geometric modeling and image reconstruction techniques that we used to constrain the brightness distribution in thermal light and scattered light as well as our companion search (Section 3). We then discuss our findings and their implications on the evolutionary state of this special object in Section 4 and summarize our results in Section 5.

## 2. Observations

### 2.1. VLT/SPHERE Polarimetric Imaging in Visible Light

MWC 614 was observed on the night of 2015 June 10 with SPHERE (Beuzit et al. 2008) as part of ESO observing program 095.C-0883 (PI: S. Kraus). SPHERE is a high-performance adaptive optics system (Fusco et al. 2014) installed on unit telescope (UT) 3 at the VLT on the top of Cerro Paranal in Chile. We used ZIMPOL (Roelfsema et al. 2014), the polarimetric imaging instrument of SPHERE operating in the visible and with two cameras. The *R*-band filters ( $\lambda_c = 645.9$  nm,  $\Delta\lambda = 56.7$  nm) were selected for both cameras, and the slow-polarimetric mode (P2) was used (see Table 1). The observations were conducted using a Lyot coronagraph (V\_CLC\_M\_WF) with an on-sky-projected diameter of 155 mas.

A polarimetry observing sequence includes observations with the half-wave plate rotated along position angles of  $0^\circ$ ,  $90^\circ$ ,  $45^\circ$ , and  $135^\circ$  to measure the Stokes  $Q$  parameter and position angles of  $22^\circ.5$ ,  $112^\circ.5$ ,  $67^\circ.5$ , and  $157^\circ.5$  for the Stokes  $U$  parameter. One sequence of observation includes two polarimetric cycles ( $Q$  and  $U$ ).

Because we were using a coronagraphic mask, we repeated this observation sequence three times with three different field rotations of  $0^\circ$ ,  $30^\circ$ , and  $60^\circ$ .

The raw data cubes were processed using the SPHERE/ZIMPOL data reduction pipeline (version 3.12.3). The output of the pipeline is cubes of  $Q^+$ ,  $Q^-$ ,  $U^+$ , and  $U^-$  Stokes components and their associated total flux intensities. We then centered the images with respect to the coronagraphic mask and derotated them using custom scripts. We constructed the Stokes  $Q$  and  $U$  parameters as follows:

$$Q = \frac{Q^+ - Q^-}{2} \quad (1)$$

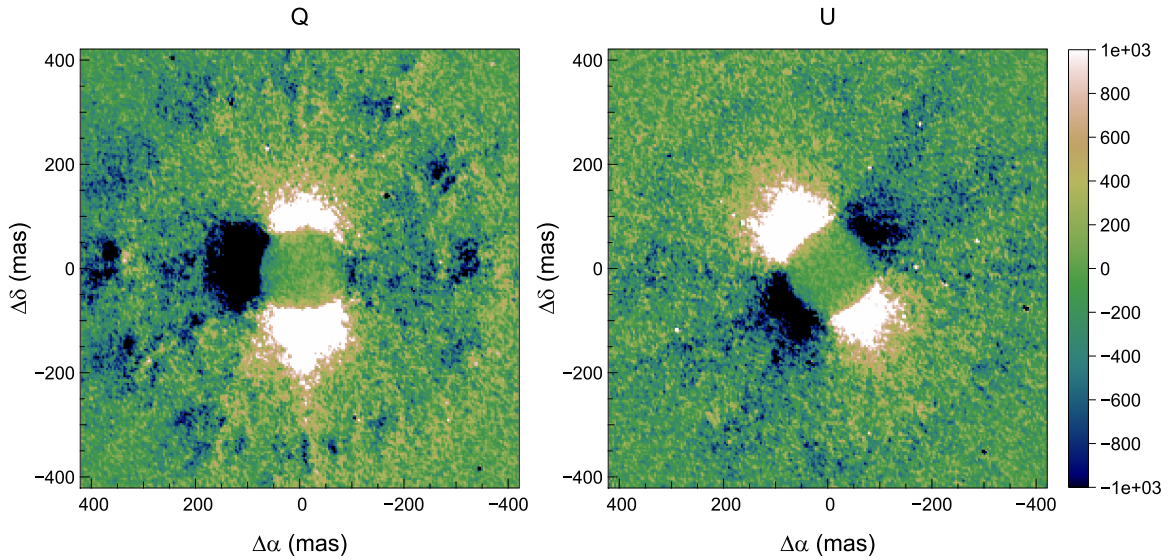


**Figure 1.** Raw polarized intensities from the SPHERE/ZIMPOL instrument for the STOKES parameters  $Q$  (left) and  $U$  (right).

**Table 1**  
Observing Log

Instrument	Date (UT)	Telescope(s)/ Configuration	Mode	Filter	NDIT $\times$ DIT	# of Pointings
SPHERE/ZIMPOL	2015 Jun 10	UT3	P2	N_R	48 $\times$ 45 s	1
NIRC2	2013 Nov 16	Keck II	SAM	H	2 $\times$ 25 $\times$ 0.845 s	1
PIONIER	2013 Jun 06	A1-G1-J3-K0	GRISM	H	...	1
	2013 Jul 04	A1-B2-C1-D0	GRISM	H	...	2
AMBER	2013 Jun 13	UT2-UT3-UT4	Low Res.	K	5000 $\times$ 26 ms	1
CLASSIC	2010 Jul 20	E1-W1	...	K	...	2
	2010 Jul 21	E1-S1	...	K	...	2
	2011 Jun 12	W1-W2	...	K	...	1
CLIMB	2011 Jun 12	E1-W1-W2	...	K	...	2
	2011 Jun 14	E1-W1-W2	...	K	...	3
	2011 Jun 16	E1-W1-W2	...	K	...	3
	2011 Jun 21	E1-W1-W2	...	K	...	2
	2011 Jun 25	E2-S1-W2	...	K	...	1
	2011 Jun 26	S1-W1-W2	...	K	...	3
	2011 Aug 04	E2-S2-W2	...	K	...	3
	2012 Jun 28	E1-E2-S1	...	K	...	3
	2012 Jun 30	E1-S1-S2	...	K	...	1
MIDI	2003 Jun 16	UT1-UT3	PRISM	N	...	3
	2004 Apr 10	UT2-UT3	PRISM	N	...	2
	2006 May 15	UT2-UT3	GRISM	N	...	1
	2006 May 16	UT1-UT3	GRISM	N	...	2
	2006 May 17	UT3-UT4	PRISM	N	...	1
	2006 Jun 11	UT3-UT4	PRISM	N	...	1
	2006 Jun 14	UT1-UT2	PRISM	N	...	2
	2006 Jul 09	UT3-UT4	PRISM	N	...	1
	2006 Jul 13	UT1-UT2	GRISM	N	...	2
	2009 Aug 14	E0-G0	PRISM	N	...	7
	2009 Aug 15	H0-G0	PRISM	N	...	3

$$U = \frac{U^+ - U^-}{2}. \quad (2)$$

As suggested by Avenhaus et al. (2014), we equalized the fluxes coming from the ordinary and extraordinary beams

(linear polarization that is parallel and perpendicular to the optical bench, respectively) for each frame and corrected for any difference in the acquisition between the Stokes  $Q$  and  $U$  parameters (we computed the efficiency of measurement of Stokes  $U$  of  $e_U = 0.986$  as in Avenhaus et al. 2014). We then

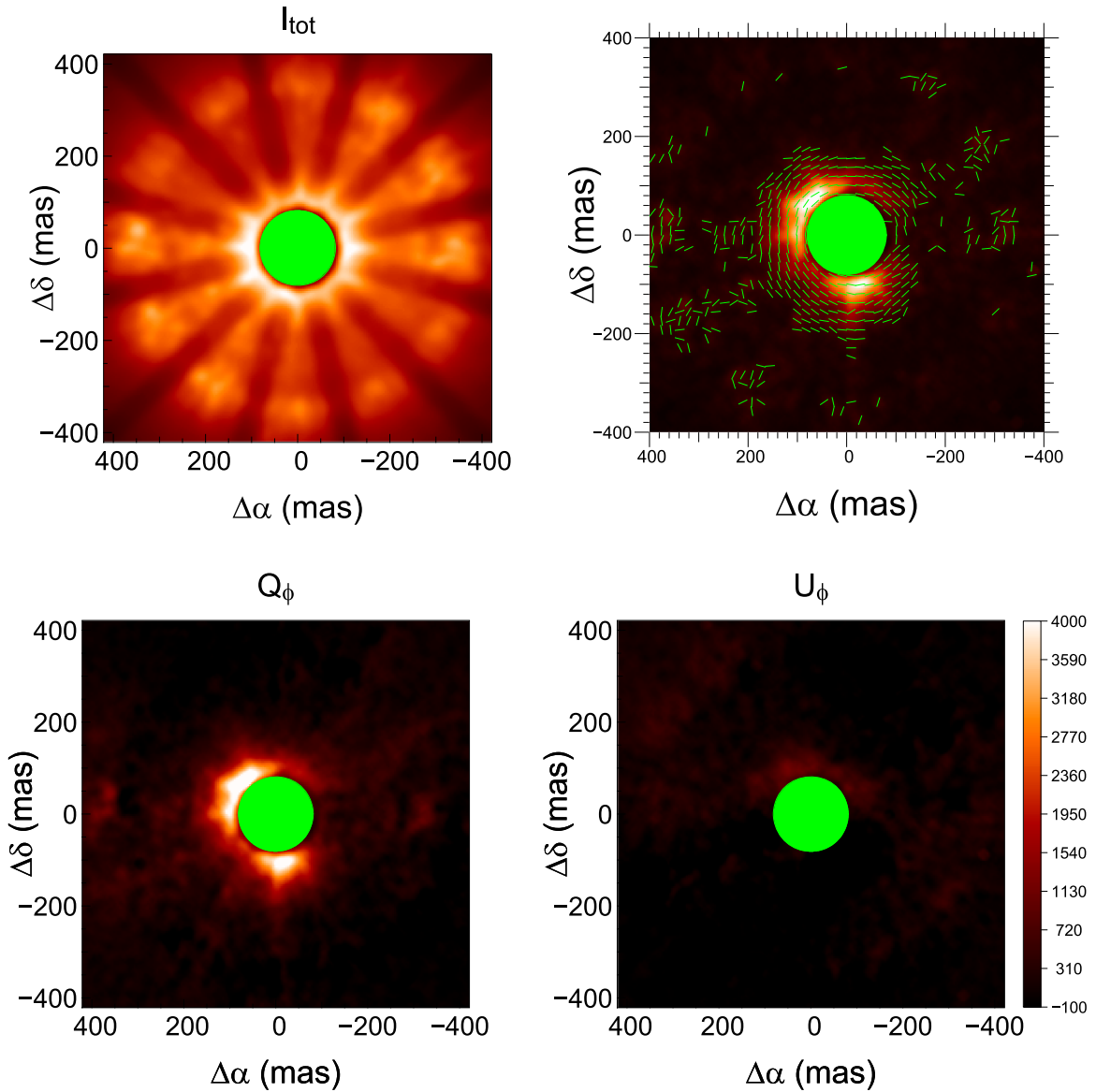


**Figure 2.** SPHERE/ZIMPOL observations of MWC 614. Top left: total intensity image, which shows the coronagraphic mask in green and the coronagraph spider arms. Top right: polarized intensity image, where the green bars represent the orientation of the polarized light. Bottom left:  $Q_\phi$  intensity image. Bottom right:  $U_\phi$  intensity image.

stacked all the centered and derotated frames to obtain the total intensity,  $Q$ , and  $U$  images (see Figure 1).

The linear polarization fraction map ( $p_L$ ) and the position angle of the electric vector ( $\theta$ ) were built using

$$p_L = \sqrt{Q^2 + U^2} \quad (3)$$

$$\theta = \frac{1}{2} \arctan \frac{U}{Q}. \quad (4)$$

We also computed the polar Stokes components ( $Q_\phi$  and  $U_\phi$ ) as described in Avenhaus et al. (2014):

$$Q_\phi = Q \cos 2\Phi + U \sin 2\Phi \quad (5)$$

$$U_\phi = -Q \sin 2\Phi + U \cos 2\Phi. \quad (6)$$

$\phi$  refers to the azimuth in polar coordinates and  $\Phi$  is the angle of a pixel ( $x, y$ ) with respect to the star ( $x_0, y_0$ ):

$$\Phi = \arctan \frac{x - x_0}{y - y_0} + \theta, \quad (7)$$

with  $\theta$  being an angle correcting for the instrumental polarization (we found  $\theta = 1^\circ.76$ ). This decomposition of the Stokes parameters was used to have one image with the polarized flux and one image with noise estimation. We show all the images in Figure 2. This representation assumes that the polarized intensity is tangential; Canovas et al. (2015) indicated that for special conditions, this assumption is not true and  $U_\phi$  can still contain astrophysical information. In our case, the  $Q_\phi$  image is almost identical to the  $p_L$  image, showing that the polarized intensity vector is mostly tangential.

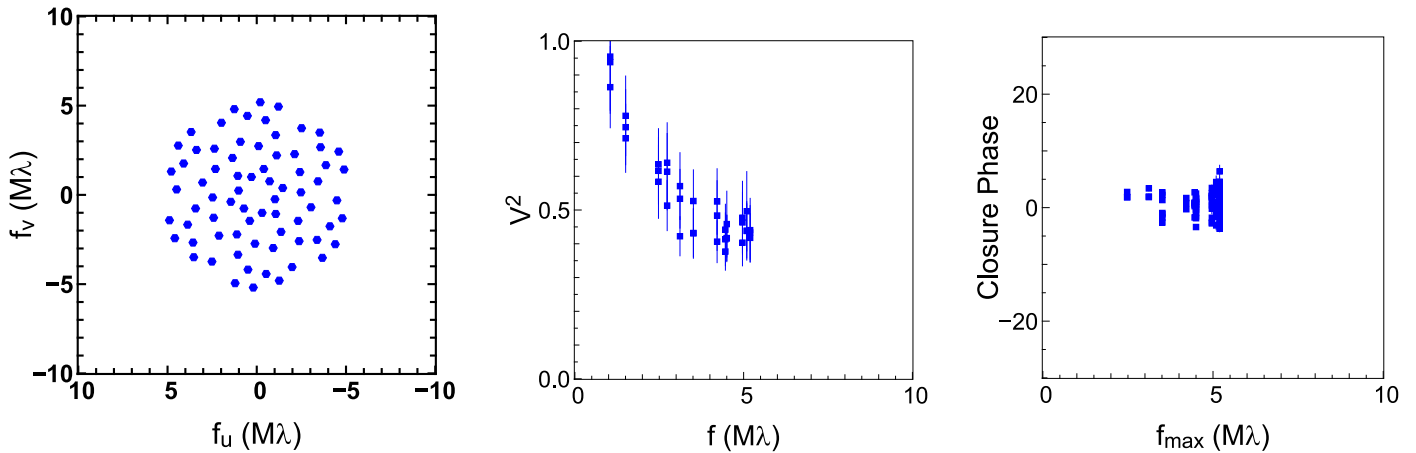


**Figure 3.** Aperture masking data set from Keck II/NIRC2 in the  $H$ -band ( $1.63 \mu\text{m}$ ). Left: the  $\{u, v\}$ -plane. Middle: squared visibilities as a function of the spatial frequency. Right: CPs as a function of the maximum spatial frequency sampled by the closed triangle of baselines.

### 2.2. Keck/NIRC2 Sparse Aperture Masking Interferometry

The sparse aperture masking (SAM) observations were taken on 2013 November 16 using the NIRC2 instrument mounted to the 10 m Keck II telescope located on the summit of MaunaKea, Hawaii. We observed MWC 614 as part of a CAL1-SCI-CAL1-SCI-CAL2 sequence where HD 178568 and HD 178332 were used as calibrators CAL1 and CAL2, respectively. We used the  $H$ -band filter ( $\lambda_c = 1.63$ ,  $\Delta\lambda = 0.33 \mu\text{m}$ ). The integration time on target totaled  $2 \times 25$  coadds  $\times 0.845$  s (see Table 1). The use of the 9-holes mask allowed us to measure 84 closure phases (CPs) and 36 squared visibilities ( $V^2$ ; see Figure 3).

The absolute level of  $V^2$  is unknown due to calibration issues, while the relative values are preserved. We describe in Appendix A.1 the method we used to calibrate these  $V^2$ . In Figure 3, we can see a drop of  $V^2$  with the spatial frequency, which indicates that the object is resolved. The CP is an indication of the degree of departure from the centrosymmetry of the object, where nonzero CPs indicate a centrosymmetric object. We measured CPs up to  $5^\circ$  (Figure 3), which clearly indicates that the object is asymmetric.

### 2.3. Infrared Long-Baseline Interferometry

#### 2.3.1. VLTI/PIONIER

One part of the interferometric data set was taken at the VLTI with the PIONIER instrument (Le Bouquin et al. 2011). PIONIER is an optical interferometric instrument combining four telescopes in the NIR ( $H$ -band centered at  $1.65 \mu\text{m}$ ). The data set was taken on 2013 June 06 and 2013 July 03 as part of the PIONIER Herbig Ae/Be Large Program (190.C-0963, see Lazareff et al. 2017). It was reduced using *pndrs* (Le Bouquin et al. 2011).

The  $\{u, v\}$  coverage (left panel of Figure 4) of the observations corresponds to a maximum reached spatial resolution of 2.3 mas and includes 66 individual measurements. The data set covers baseline lengths ranging from 7 to 140 m and is fully described in Lazareff et al. (2017) (see also Table 1).

The PIONIER  $V^2$  and CP are presented in the bottom left and right panels of Figure 4, where the different colors represent different channels (from blue, for  $1.6 \mu\text{m}$ , to red, for  $1.83 \mu\text{m}$ ). We see that at a given baseline there is a decrease of the  $V^2$

with increasing wavelengths. This is due to the chromatic effect that arises from the temperature difference between the star and its circumstellar environment (Kluska et al. 2014). In addition, the  $V^2$  measurements show a plateau indicating that the circumstellar structure is already overresolved (larger than the smallest probed spatial frequency, which corresponds to an angular resolution of 40 mas). The CP signal does not seem to indicate any departure from point symmetry.

#### 2.3.2. VLTI/AMBER

MWC 614 was also observed with AMBER, which is a VLTI three-telescope beam combiner working in the  $K$ -band (centered on  $2.2 \mu\text{m}$ ; Petrov et al. 2007). The observations were conducted on 2011 June 13 as part of ESO observing program 087.C-0498(A) (PI S. Kraus). We used the 8.2 m VLTI UTs in the UT2-UT3-UT4 configuration, which provided baseline lengths of between 30 and 80 m (see Table 1). Employing AMBER’s low-resolution mode, our observations covered the  $K$ -band with a spectral resolution of  $R = 30$ . We recorded a total of 5000 interferograms with a detector integration time of 26 ms and extracted visibilities and CPs using the *amdlb* software (Release 3; Tatulli et al. 2007; Chelli et al. 2009). We followed the standard AMBER data reduction procedure and selected the interferograms with the 10% best signal-to-noise ratio with the goal to minimize the effect of residual telescope jitter.

The  $V^2$  profile measured with AMBER shows a plateau (bottom left panel of Figure 5), indicating that the extended component that is also seen with PIONIER (Figure 4) and NIRC2 (Figure 3) is also overresolved in the  $K$ -band.

#### 2.3.3. VLTI/MIDI

For our interpretation we also include archival MIDI observations on MWC 614 that were presented in Menu et al. (2015). MIDI is an interferometric instrument combining light from two telescopes in the MIR ( $8\text{--}13 \mu\text{m}$ ; Leinert et al. 2003). This data set consists of 27 individual observations with baseline lengths ranging from 10 to 90 m (see Table 1).

#### 2.3.4. CHARA/CLIMB and CHARA/CLASSIC

Longer baseline interferometric observations of MWC 614 were obtained using the Center for High Angular Resolution

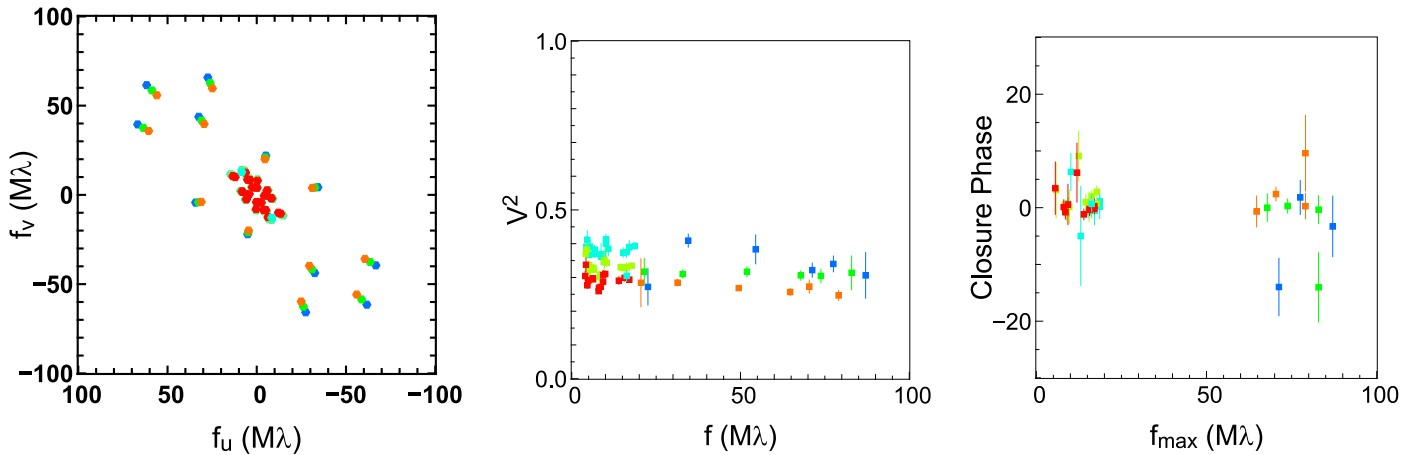


**Figure 4.** The same as Figure 3 but for the VLTI/PIONIER data set in the  $H$ -band. The colors indicate the different wavelengths from  $1.60 \mu\text{m}$  (blue) to  $1.79 \mu\text{m}$  (red).

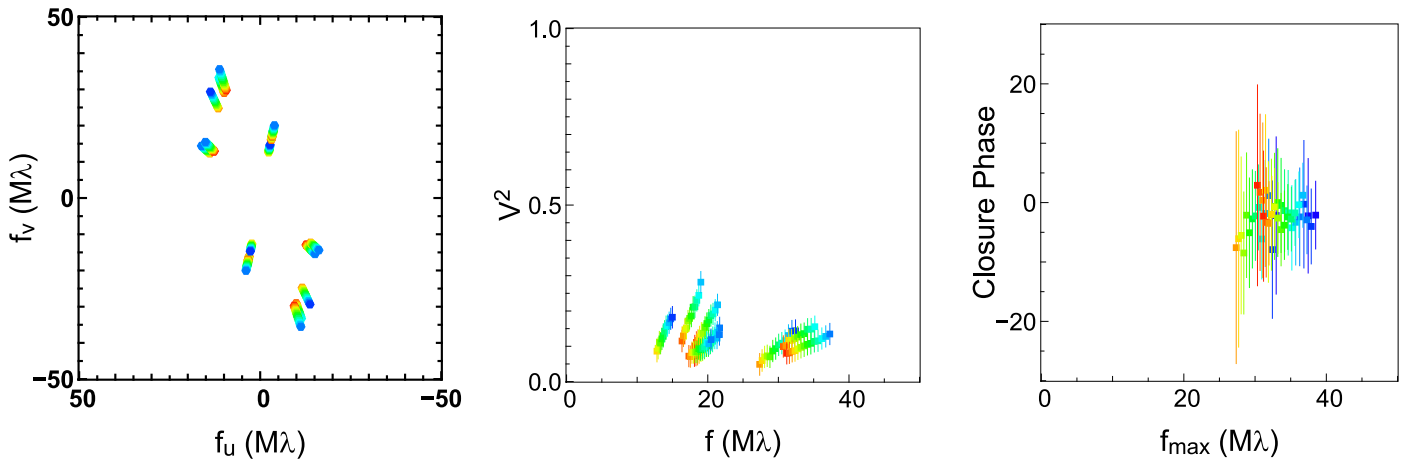


**Figure 5.** The same as Figure 3 but for the VLTI/AMBER data set in  $K$ -band. The colors indicate the different wavelengths from  $2.1 \mu\text{m}$  (blue) to  $2.5 \mu\text{m}$  (red).

Astronomy (CHARA) Array over a 2-yr period between 2010 July 20 and 2012 June 30. The CHARA Array is a Y-shaped array consisting of six 1 m-class telescopes located at Mount Wilson Observatory. The CLASSIC two-telescope and CLIMB three-telescope beam combiners (ten Brummelaar et al. 2013) were used to obtain  $K$ -band ( $\lambda_c = 2.13 \mu\text{m}$ ) interferometric fringes on a variety of telescope configurations covering baseline lengths from 33 to 329 m. The total data set consists of six  $V^2$  measurements from CLASSIC and 119  $V^2$  and 17 CP measurements from CLIMB (see Table 1 and Figure 6).

The CLASSIC and CLIMB data were reduced using a pipeline developed at the University of Michigan that is better suited to recover faint fringes for low-visibility data than the standard reduction pipeline of ten Brummelaar et al. (2012). All data that showed no clear signs of being affected by instrumentation or observational effects (e.g., drifting scans or flux dropout on one or more telescopes) were retained in the data reduction process. Particular attention was given to instances where drift or low signal-to-noise dominated the majority of scans during data acquisition on a particular baseline pair but observation notes were clear that fringes were present during the data acquisition. In these cases, the affected scans were carefully flagged while the power spectrum,

averaged over the retained data, was inspected for a signal. This procedure resulted in an improved noise estimation for the data set. The observed visibilities and CPs were calibrated using the standard stars selected with JMMC SearchCal (HD 178568: uniform disk [UD] diameter =  $0.127 \pm 0.01$  mas; HD 177305: UD diameter =  $0.25 \pm 0.05$  mas; HD 178332: UD diameter =  $0.178 \pm 0.013$  mas; HD 178379: UD diameter =  $0.216 \pm 0.015$  mas; HD 179586: UD diameter =  $0.193 \pm 0.014$  mas; HD 181253: UD diameter =  $0.238 \pm 0.017$  mas; HD 189509: UD diameter =  $0.26 \pm 0.02$  mas).

### 3. Disk Geometry and Companion Search

We constrain the morphology of the emission by fitting geometrical models to our extensive data set, in polarized light, NIR thermal emission, and MIR thermal emission. We also perform a companion search on a part of the CHARA/CLIMB data set.

#### 3.1. Scattered Light Emission

The SPHERE/ZIMPOL image (Figure 2) shows two patches of flux coming from the east and the south just outside the

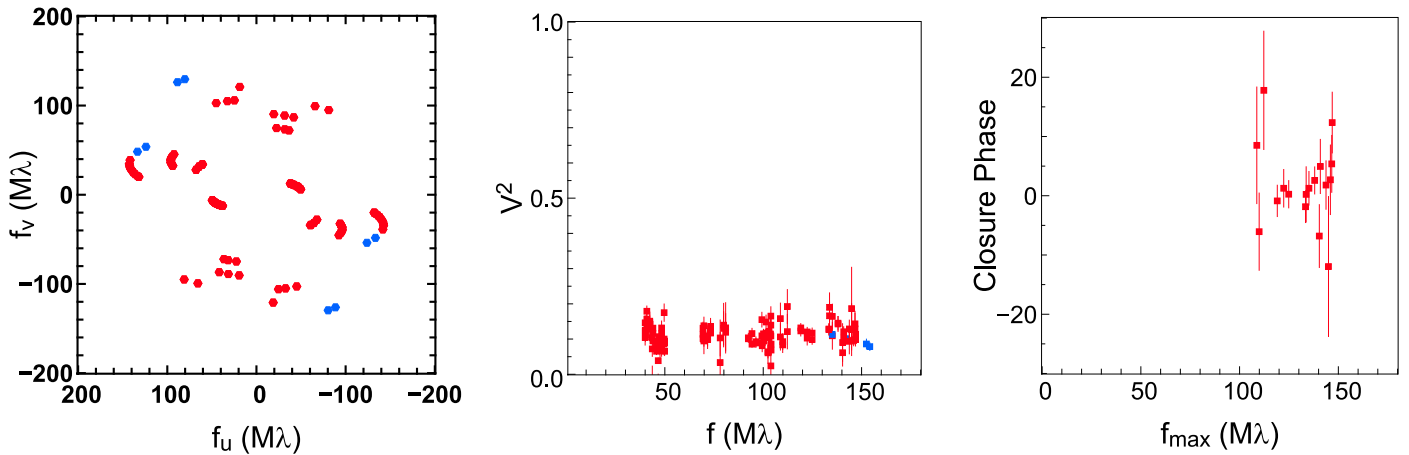


**Figure 6.** The same as Figure 3 but for the CHARA/CLASSIC (blue) and CHARA/CLIMB (red) data set in the  $K$ -band. These observations were conducted in one channel at  $2.13 \mu\text{m}$ .

coronagraphic mask. The east patch is more luminous and more extended. In the context of the stellar light scattered on the disk surface, these patches are related and can be interpreted as coming from an inclined disk where we see only one side (the northwestern side is not illuminated).

In order to reproduce this emission geometry we used geometric models of a centered Gaussian, an off-center Gaussian, and a skewed Gaussian ring to reproduce the disk surface. The models are fully described in Appendix A.2. Our Gaussian models consist of a Gaussian defined by its full width half maximum (FWHM;  $w$ ). This two-dimensional Gaussian model has a minor-to-major axis ratio of  $\cos i$  and a position angle ( $\theta$ ) defined from north to east. In the off-centered case, this Gaussian can be shifted east and north with respect to the star by  $x_*$  and  $y_*$ . The skewed ring is defined by an infinitesimal ring with a radius ( $R$ ), an inclination ( $i$ ), and a position angle ( $\theta$ ). It is modulated azimuthally by a sine function starting at a major axis and with an amplitude of  $s$  ( $-1 < s < 1$ ). Finally, the ring is convolved by a Gaussian with an FWHM of  $w$ .

We show the best-fit model image in Figure 7 and list the corresponding parameters in Table 2. The coronagraphic mask sets our inner working angle to  $\sim 150$  mas, which prevents us from constraining the inner disk radius reliably.

The  $\chi^2$  are normalized to the best-fit model. The centered Gaussian model is the simplest model but also has the worst  $\chi^2_{\text{norm}}$ , two times larger than the two other ones. It means that as expected, the flux is larger on one side of the coronagraph than on the other. The two models reproducing this asymmetry have a very similar  $\chi^2_{\text{norm}}$ . The best-fitting model is the off-center Gaussian model, with a 30 mas separation along the direction of  $105^\circ$ . The second model, which well reproduces this asymmetry, is the skewed ring model. The skewness ( $s = 0.53 \pm 0.01$ ) mimics the radiative transfer effects of an inclined disk (e.g., Lazareff et al. 2017).

Keeping in mind the disk interpretation, we can compare the sizes and orientations of the two best models. The size of the Gaussian is  $252.1 \pm 1.1$  mas. The ring model has a radius of  $55.7 \pm 6.3$  mas and a Gaussian width of  $205 \pm 8.1$  mas. The large error bars are due to the coronagraphic mask that does not allow us to probe the inner parts of the disk, creating a degeneracy between the radius and the Gaussian width of the ring. The inclinations of both the Gaussian ( $i = 47.4 \pm 0.3$ ) and the skewed ring ( $i = 41.4 \pm 0.7$ ) are different at  $8.5\sigma$ .

The disk position angle ( $\theta$ ) indicates roughly (at  $8\sigma$ ) the same orientation for the major axis ( $\theta = 24.8 \pm 0.4$  and  $\theta = 21.5 \pm 0.4$ ) for the Gaussian and the skewed ring, respectively.

### 3.2. MIR Thermal Emission

The inner disk region is not resolved by SPHERE observations as it is inside the region covered by the coronagraph. In order to characterize the disk gap we analyzed archival MIDI data, which traces dust at temperatures of  $\gtrsim 300$  K. This data set is more complete than the one in Fedele et al. (2008) and we therefore expected to probe the disk geometry in more detail.

The visibility data present several lobes that seem inconsistent with a Gaussian structure. These lobes could be produced by a Bessel function that is the Fourier transform of a sharp ring. We therefore decided to fit both a Gaussian and a Gaussian ring model. The best-fit parameters are presented in Table 3 with the error bars computed using a bootstrap method.

The Gaussian model differs from the Gaussian ring by setting the radius of the ring to 0. The Gaussian model does not reproduce the data set very well—it has a reduced  $\chi^2$  of 3.43. We can see that the orientation parameters are not well constrained (an error bar of  $12.1$  on the inclination and  $27.2$  on the position angle).

The Gaussian ring fit reproduces the visibility curve in a better way (see Figure 8) with a reduced  $\chi^2$  of 1.61. We can see that the ring radius is about  $41.8 \pm 0.9$  mas. The ring orientations ( $i = 52.5 \pm 6.1$ , PA =  $26.4 \pm 6.2$ ) are consistent with the ones derived from the SPHERE/ZIMPOL image ( $i = 41.4 \pm 0.7$ , PA =  $32.3 \pm 1.0$ ) and previous work ( $i = 57^\circ \pm 2^\circ$ , PA =  $23^\circ \pm 3^\circ$ ; Fedele et al. 2008). From the best-fit model the central point source contribution (that can be interpreted as the stellar contribution) is very low ( $2.7\% \pm 0.9\%$ ), at  $3\text{-}\sigma$  from a  $0\%$  contribution. This is different from the  $20\%$  contribution of unresolved emission as fitted by Fedele et al. (2008).

We can verify the orientation of the best Gaussian ring fit by transforming the baseline length to the effective baseline length corrected for the inclination and position angle of the best fit (i.e.,  $i = 52.5$  and PA =  $26.4$ ). In Figure 9 we can see that the data points align well and form a Bessel-like function. Note also that the best fit follows the general trend of this profile

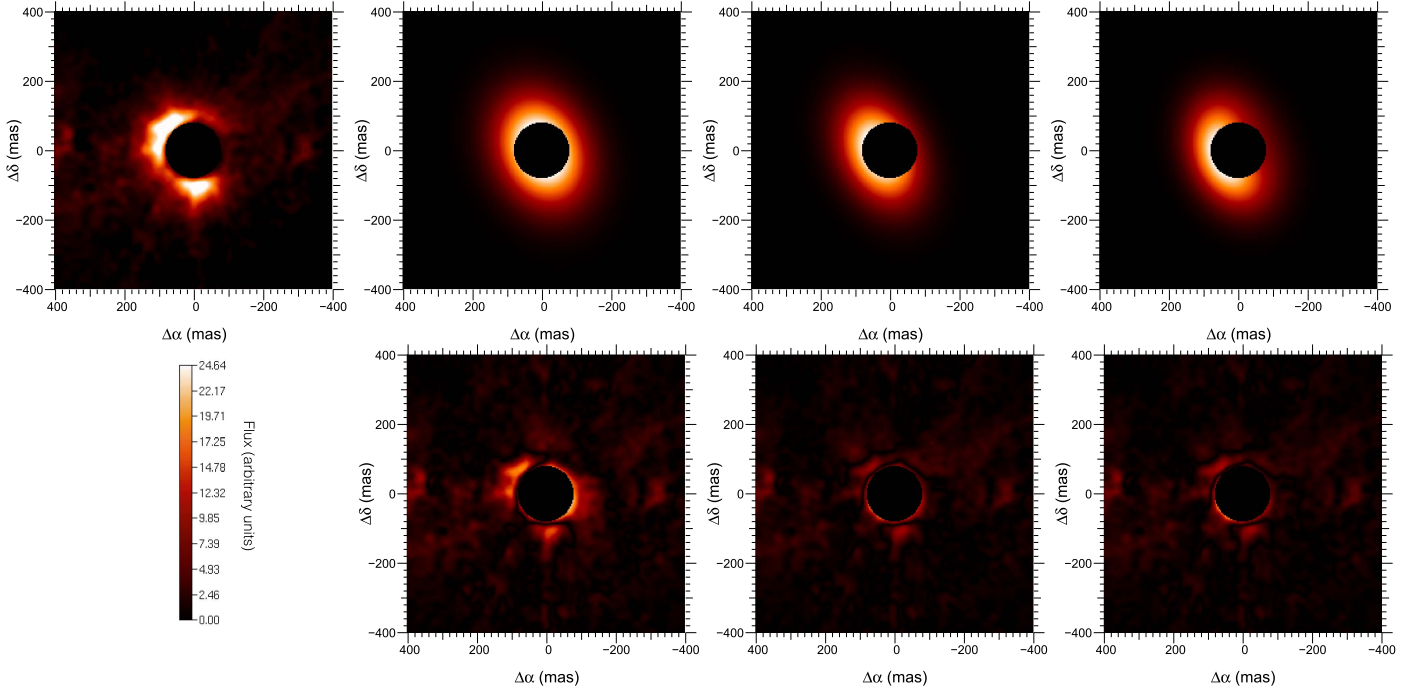


**Figure 7.** Images of the fit to the SPHERE data. Top row, left to right: SPHERE image, best-fit model images with the coronagraph for the centered Gaussian, the off-center Gaussian, and the skewed Gaussian ring, respectively. Bottom row, from left to right: residuals to the centered Gaussian, the off-center Gaussian, and the skewed Gaussian ring, respectively.

**Table 2**

Best-Fit Model Parameters to the SPHERE Image

Model	Centered Gaussian	Off-center Gaussian	Skewed Ring
$\chi^2_{\text{norm}}$	2.01	1.02	1.00
Param.	Value $\pm$ Err	Value $\pm$ Err	Value $\pm$ Err
$R$ [mas]	...	...	$55.7 \pm 6.3$
$w$ [mas]	$259.0 \pm 1.7$	$252.1 \pm 1.1$	$205.0 \pm 8.1$
$i$ [ $^\circ$ ]	$40.5 \pm 0.5$	$47.4 \pm 0.3$	$41.4 \pm 0.7$
$\theta$ [ $^\circ$ ]	$23.7 \pm 0.9$	$24.8 \pm 0.4$	$21.5 \pm 0.4$
$s$	...	...	$0.53 \pm 0.01$
$x_*$ [mas]	...	$29.7 \pm 0.3$	...
$y_*$ [mas]	...	$-5.4 \pm 0.4$	...

**Table 3**

Best-Fit Models to the MIDI Data Set

Model	Gaussian	Gaussian Ring
$\chi^2$	3.43	1.61
$F_*^{10\mu\text{m}}$	$4.4 \pm 1.0\%$	$2.7 \pm 0.9\%$
$R$ [mas]	0	$41.8 \pm 0.9$
$w$ [mas]	$92.4 \pm 27.7$	$18.6 \pm 8.8$
$i$ [ $^\circ$ ]	$74.2 \pm 12.1$	$52.5 \pm 6.1$
$\theta$ [ $^\circ$ ]	$23.2 \pm 27.2$	$26.4 \pm 6.2$

even though the visibility level from our model is too low for the longest baselines.

### 3.3. NIR Thermal Emission

In order to probe the geometry of the innermost regions of the disk ( $<10$  au) we use a similar model that was used in Section 3.2, adding some parameters that are probed by the

NIR data set. We also use the image reconstruction technique to recover the intensity distribution for the data set with the best-sampled  $\{u, v\}$ -plane, which is the SAM data set.

#### 3.3.1. Model Fitting

After normalizing the short-baseline SAM visibility data (see Appendix A.1), we fit our analytic disk model to the NIR interferometric data sets. The model consists of a point source representing the star and a Gaussian that represents the dusty environment of the star. The star can be shifted with respect to the Gaussian to reproduce the nonzero CP signal seen in the aperture masking data set (see Figure 3, right panel). The details of the model are presented in Appendix A.3.

We first applied our model to the aperture masking data only, as this data set alone constrains the size of the extended emitting region. We then successively added the PIONIER data set (which covers the same band as the aperture masking data) and the longer-wavelength AMBER and CHARA data as the final step. Because the SAM  $V^2$  data sets the size and orientation of the emission and because it has large error bars, we increased its weight in the fitting by a factor of 25 (corresponding to artificially reducing its error bars by a factor of 5). The best-fit results for these three fits are presented in Table 4 and the corresponding model images appear in Figure 10. The  $V^2$  and CPs from the models are shown in Figures 18 and 19 in the Appendix.

We can see that a similar disk orientation is found for the different model fits: inclinations between  $51^\circ$  and  $58^\circ$ , and position angles between  $25^\circ$  and  $31^\circ$ . These numbers are in very good agreement (within 1 or 2- $\sigma$  for the inclination and less than 1- $\sigma$  for the position angle) with the orientations derived from the SPHERE image in Section 3.1 and the MIDI data set in Section 3.2.

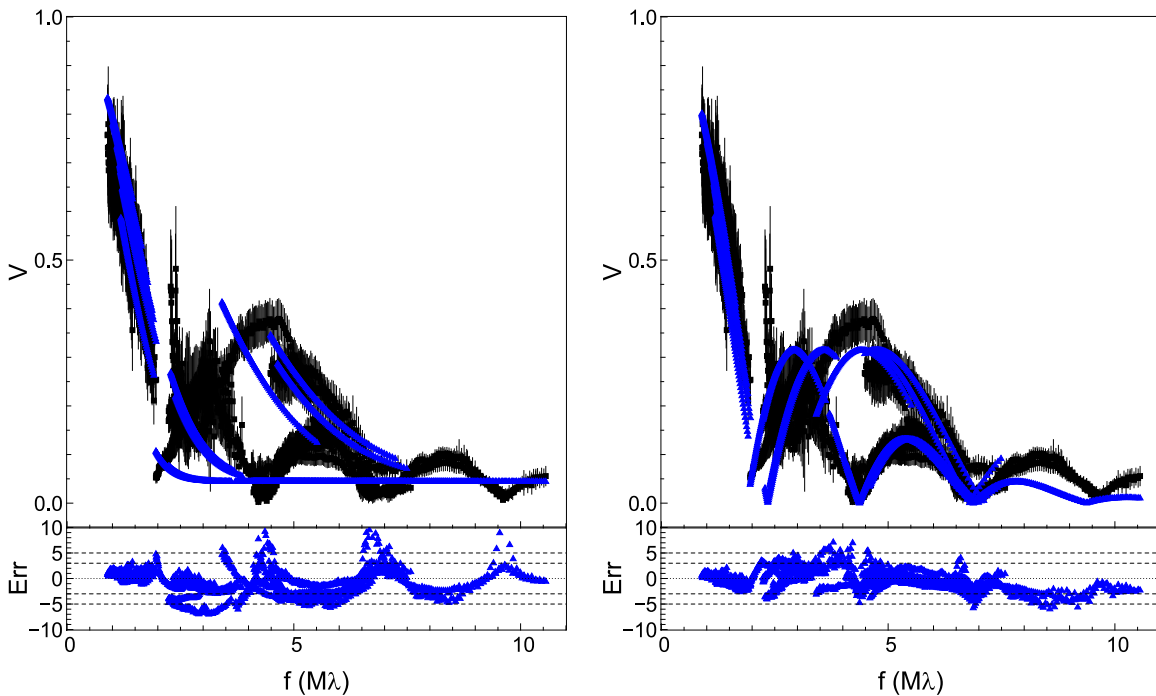


**Figure 8.** Fit to the MIDI visibilities between 8 and 12  $\mu\text{m}$ . Left: the Gaussian model. Right: the Gaussian ring model. The data set is in black squares and the model is in blue triangles. Bottom panels: the residuals.

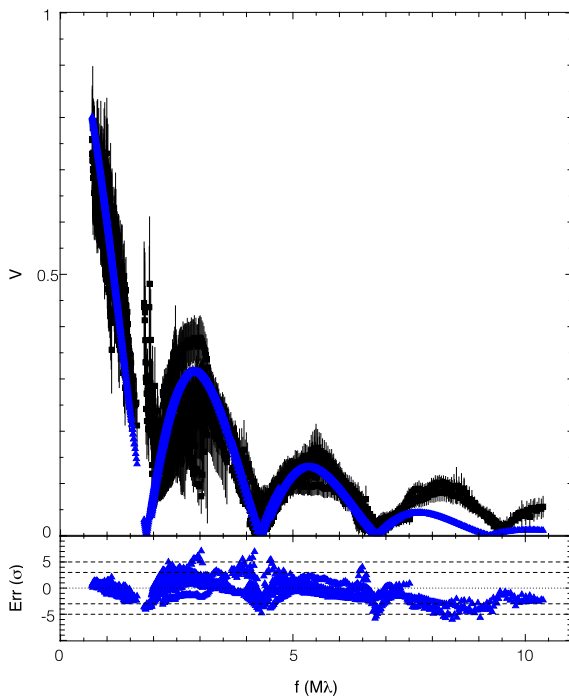


**Figure 9.** The MIDI visibilities (black squares) and the Gaussian ring best fit (blue triangles) vs. the effective baseline, i.e., the baseline that is oriented to match the inclination and position angle of the best-fit Gaussian ring model ( $i = 52^\circ$  and  $\text{PA} = 26^\circ$ ). The visibility profile shows a clear Bessel-like function.

From the squared visibility fit, a Gaussian-like geometry seems to suit the global shape of the NIR circumstellar emission. The derived FWHM of  $\approx 50$  mas is consistent between the different fits. The size is well constrained, in particular at the PIONIER, AMBER, and CHARA baselines where the environment is fully resolved. The emission is therefore smoothly distributed and does not show a clear

rim-like profile as in the MIDI observations tracing cooler disk regions at longer wavelengths (where the different lobes coming from a Bessel function indicate a sharp morphology; see Section 2.3.3).

The stellar-to-total flux ratio at 1.65  $\mu\text{m}$  ( $F_*^{1.65 \mu\text{m}}$ ) shows a rise of about 10% between the SAM fit and the three other fits. This is because this ratio is well constrained once the visibilities reach the overresolved regime, which is the case for the PIONIER, AMBER, and CHARA data sets. At spatial frequencies of over 5  $\text{M}\lambda$  (corresponding to baselines  $\gtrsim 10$  m at 1.65  $\mu\text{m}$ ), the extended component is overresolved and the flux ratio can be constrained very tightly from the plateau level in the visibility, if the long-baseline data are included. The best fits to the SAM+PIONIER, SAM+PIONIER+AMBER, and SAM+PIONIER+CHARA data agree on a value of  $F_*^{1.65 \mu\text{m}} \sim 59 \pm 0.6\%$  of unresolved flux at 1.65  $\mu\text{m}$ .

The spectral dispersion of the  $H$ -band PIONIER and  $K$ -band AMBER and CHARA data sets and the span across two bands for the whole long-baseline data set allow us to probe the temperature of the environment assuming that the star is in the Rayleigh–Jeans regime. Our fit indicates a temperature of  $\sim 1800$  K, with  $F_\lambda^* \propto \lambda^{-4}$  for the SAM+PIONIER and the SAM+PIONIER+AMBER data sets ( $T = 1719 \pm 154$  K and  $T = 1812 \pm 71$  K, respectively). However, the best fit to the SAM+PIONIER+AMBER+CHARA data set indicates a lower temperature ( $T = 1407 \pm 26$  K).

Significant deviations from zero CPs are observed in the SAM data, suggesting that the brightness distribution is nonaxisymmetric. The only model parameters that produce a nonzero CP signal are the coordinates of the central star ( $x_*$  and  $y_*$ ) relative to the center of the inclined Gaussian. We notice the high  $\chi^2$  for the fit of the SAM data set and that the CPs are not well fitted by the four models (Figure 18 in the Appendix). This suggests a more complex geometry for the NIR emission.

**Table 4**  
Parameters of the Best-fit Gaussian Model to Our Various Data Sets

Parameters	SAM	SAM+PIONIER	SAM+PIONIER+AMBER	All
$\chi^2$	20.4	9.3	8.4	6.3
$\chi^2_{v2}$	0.3	0.1	0.1	0.1
$\chi^2_{CP}$	53.5	15.9	17.0	14.6
$F_*^{1.65 \mu\text{m}}$ [%]	$48.9 \pm 3.1$	$59.8 \pm 0.6$	$59.0 \pm 0.4$	$59.5 \pm 0.4$
$w$ [mas]	$55.6 \pm 22.1$	$52.0 \pm 6.4$	$47.7 \pm 2.4$	$51.0 \pm 2.4$
$i$ [°]	$58.0 \pm 11.3$	$52.9 \pm 7.7$	$51.3 \pm 3.6$	$54.8 \pm 3.0$
$\theta$ [°]	$28.0 \pm 5.9$	$31.1 \pm 22.1$	$26.3 \pm 3.6$	$25.5 \pm 2.6$
$T$ [K]	...	$1719 \pm 154$	$1812 \pm 71$	$1435 \pm 28$
$x_*$ [mas]	$-1.05 \pm 0.71$	$-1.58 \pm 0.49$	$-0.80 \pm 0.11$	$0.81 \pm 0.09$
$y_*$ [mas]	$-0.61 \pm 1.02$	$-1.38 \pm 0.48$	$-0.12 \pm 0.05$	$0.11 \pm 0.04$

### 3.3.2. Image Reconstruction

Another approach to determine the emission morphology is to reconstruct an image using aperture synthesis methods. This approach remains model independent and is more likely to be able to fit the CPs that were seen in the aperture masking data and that were not reproduced by the parametric model. We reconstruct an image from the SAM data set alone, as this data set provides a rather uniform  $\{u, v\}$ -coverage. Adding the PIONIER and AMBER data sets would introduce artifacts in the image reconstruction, as the Fourier plane coverage is relatively poor in these cases. We carry out the image reconstruction using the *MIRA* software package (Thiébaud 2008) together with the SPARCO technique (Kluska et al. 2014) that separates the star from the image of its environment using the linearity of the Fourier transform. We use a quadratic smoothness regularization and determine the regularization weight ( $\mu$ ) using the L-curve method (Kluska et al. 2016; Willson et al. 2016), which yields the best-fit value  $\mu = 9 \times 10^9$ . When determining this value, we set the star/disk flux ratio to the level determined by the parametric models (i.e.,  $F_*^{1.65 \mu\text{m}} = 59.0\%$ ).

Our reconstructed image is shown in Figure 10. The image has a reduced  $\chi^2 = 1.2$ . The general size and orientation of the structure seen in the image is similar to the one found in the parametric models. However, the image also reveals spiral features that seem to extend from the major axis of the disk. To assess the significance of the features seen in the image we used the bootstrap method, where we reconstructed images from 500 new data sets built by drawing baselines and triangles from the full data set (see Kluska et al. 2016). Figure 11 shows the average image computed for all the bootstrap reconstructions together with contours corresponding to the pixel significance levels. The spiral features are significant up to a level of  $3\text{-}\sigma$ , making them marginally significant.

In contrast to the parametric models, the image reconstruction can reproduce the measured CP signals reasonably well. To see which parts of the image influence the CP signal we produced an asymmetry map, which was computed by subtracting the  $180^\circ$  rotated image from the original image (Kluska et al. 2016). The asymmetry map is shown in Figure 11 and reveals that the CP signal is mainly caused by the northwestern disk region. This part is located on one side from the major axis indicating inclination effects, even though this axis is misaligned slightly (by  $\sim 15^\circ$ ) with respect to the disk major axis determined in Section 3.3.1.

### 3.4. Companion Detection Limits Inside the Cavity

In order to understand the disk structure we used the NIR interferometric data to search for a companion inside the disk cavity. We applied the statistical method described in Absil et al. (2011) to derive detection limits on each of our interferometric data sets separately. In our computation we took into account the bandwidth smearing effect, which may significantly affect our longest-baseline data. As we probed the inner regions ( $< 10$  au) around the star, a companion would have moved notably between two observations that were taken several months apart. Therefore, we selected the CHARA data set taken between 2011 June 12 and 2011 August 04, as these observations were taken in a sufficiently short period but still offer good  $\{u, v\}$ -plane coverage.

First, we needed to compute the reference model without a companion that would serve as the null hypothesis. For SAM data the null scenario is the best-fit model from Section 3.3.1. For the PIONIER and AMBER data we fitted a chromatic model including a star and a background with a given temperature. For the CLIMB data we fitted a monochromatic model since there is only one spectral channel. The best-fit parameters are shown in Table 5.

In the second step, we computed a grid on the positions and contrasts of a potential companion and determined the significance at the global minimum of the fit to each data set. The  $\chi^2$  improvements compared to the null models have a low significance (1.8, 1.3, 1.6, and  $2.3\text{-}\sigma$  for PIONIER, SAM, AMBER, and CLIMB, respectively). None of the data set contains a significant detection. Finally, we derived the detection limits at the  $3\text{-}\sigma$  level for each data set (see Figure 12). We also used the disk orientation derived in earlier sections of this paper (using  $i = 52^\circ.5$  and  $\theta = 26^\circ.4$ ) to represent the detection limit in the *H*- and *K*-bands as a function of the physical distance to the central star (see Figure 13). This resulted in upper limits of  $\sim 3\%$  and  $\sim 5\%$  in the *H*-band and the *K*-band, respectively.

## 4. Discussion

Here we discuss the global structure of the disk around MWC 614 as deduced from our multiwavelength interferometric observations.

### 4.1. MIR Thermal Emission from the Inner Wall of the Outer Disk

The fit of the MIDI visibilities shows that the data are compatible with a Gaussian ring with a radius of

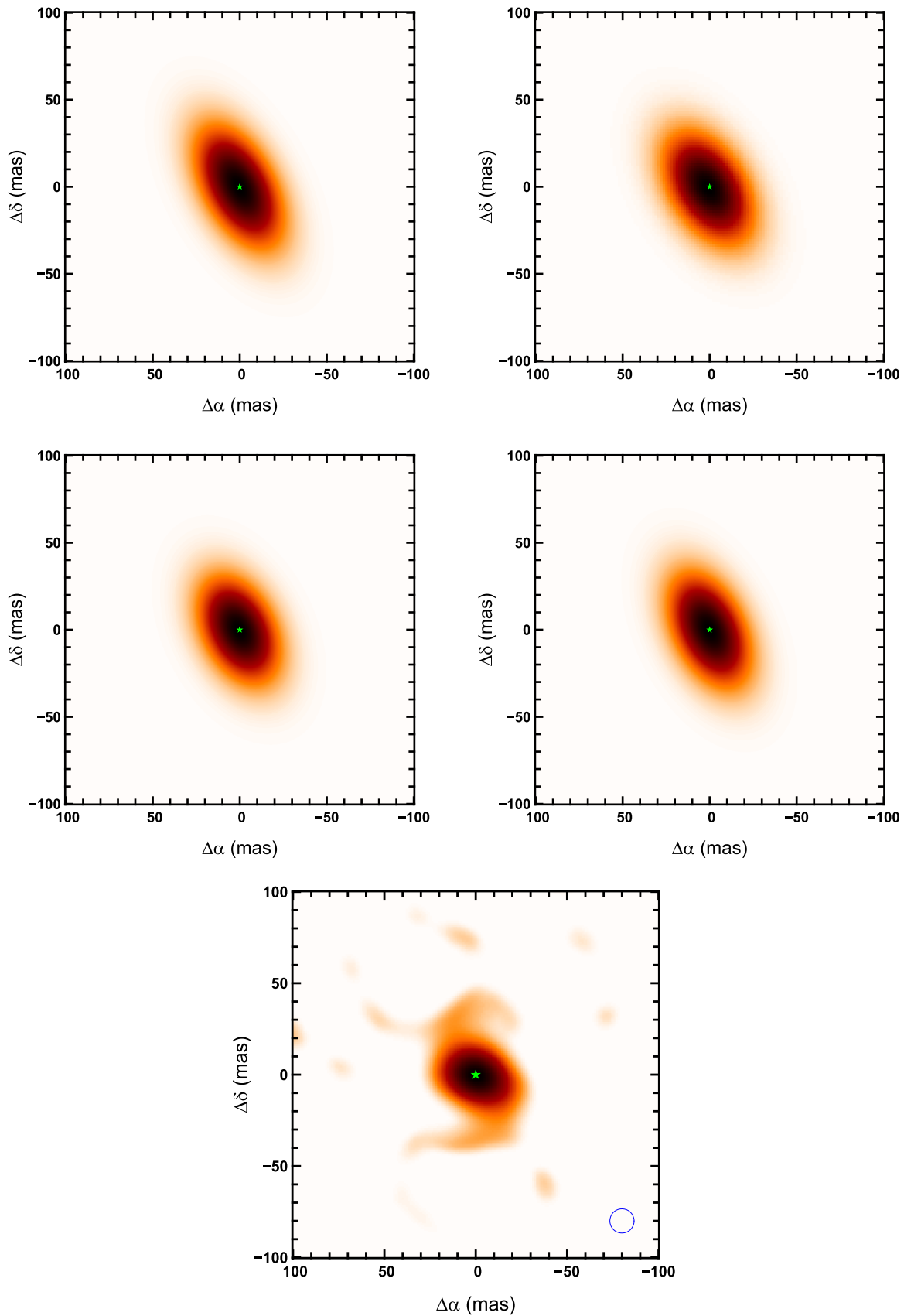


**Figure 10.** Model images that correspond to our best-fit models fitted to the following data sets. Top left: SAM. Top right: SAM+PIONIER. Middle left: SAM+PIONIER+AMBER. Middle right: SAM+PIONIER+AMBER+CHARA. Bottom: the image reconstruction on the SAM data. The green star represents the position of the star and the blue solid contour represents the beam size.

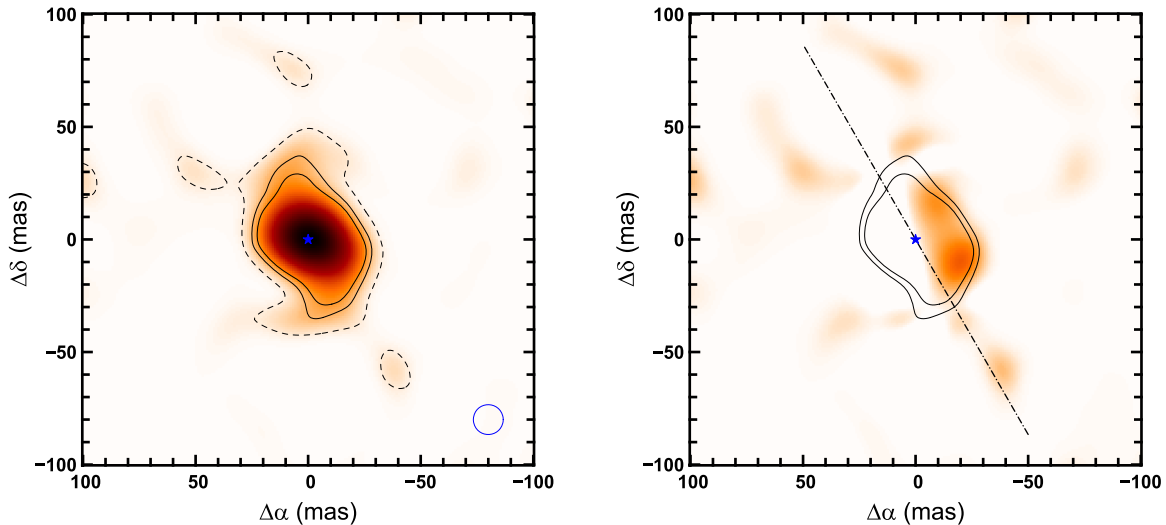


**Figure 11.** Analysis of the reconstructed image. Left: average image reconstruction built from the bootstrap method. The green star represents the position of the star; the solid and dashed lines are the 5, 3 and 1- $\sigma$  significance contours; and the blue solid contour represents the beam size. Right: the asymmetry map (see text) with contours of the original image at a 3 and 5- $\sigma$  significance overlaid. The green star represents the star and the dashed line represents the major axis.

**Table 5**  
Best Parameters for the Null Hypothesis

	PIONIER	AMBER	CLIMB	
$\chi^2$	7.4	1.0	2.7	
Param.	Value $\pm$ Err	Param.	Value $\pm$ Err	Value $\pm$ Err
$F_*^{1.65 \mu\text{m}}$ [%]	$60.3 \pm 0.3$	$F_*^{2.13 \mu\text{m}}$ [%]	$40.9 \pm 0.8$	$32.7 \pm 0.1$
$T_{\text{env}}$ [K]	$1680 \pm 79$	$T_{\text{env}}$ [K]	$1580 \pm 144$	...

$41.8 \pm 0.9$  mas corresponding to  $10.2 \pm 0.2$  au. This can correspond to the thermal emission from the disk wall. The Gaussian width of the ring corresponds to  $4.5 \pm 2.1$  au. It can be interpreted as the rim scale-height. At this distance from the star it translates into a scale-height of  $z/r$  of 0.27. This is rather high compared to other objects' morphology where typical values of  $0.1 \sim 0.15$  are attributed (e.g., Benisty et al. 2010; Mulders et al. 2013; Matter et al. 2016). It is therefore more likely that the extension of the emission is due to a radially extended emission, possibly due to a rounded rim (Mulders et al. 2013).

#### 4.2. Physical Origin of the Extended NIR Emission

The FWHM of the  $H$ -band NIR emission is around 55 mas, corresponding to about 16 au. Using this size measurement, we plotted MWC 614 in the size–luminosity diagram for young stellar objects (Figure 14, left). Earlier surveys revealed that for Herbig Ae/Be stars, the NIR size of most protoplanetary disks scales roughly with the square-root of the stellar luminosity ( $L_\odot$ ), which was interpreted as evidence that this emission primarily traces thermal emission from near the dust sublimation rim (e.g., Monnier & Millan-Gabet 2002; Monnier et al. 2005; Lazareff et al. 2017).

On the size–luminosity diagram (Figure 14) MWC 614 appears as an extreme outlier. Its radial extension ( $w/2 \sim 8$  au) is 40 times larger than the expected size of the dust sublimation radius (0.2 au, using Equation [14] in Lazareff et al. 2017, assuming a sublimation temperature of  $T_{\text{sub}} = 1800$  K, a cooling efficiency of  $\epsilon = 1$ , and a backwarming factor of

$Q_{\text{bw}} = 1$ ). Using the same equation, at 13 au the dust should have a temperature of  $\sim 350$  K, which is not compatible with the temperature we derived from the SAM+PIONIER +AMBER data sets ( $T = 1812 \pm 71$  K; Section 3.3.1). Therefore, we argue that the NIR emission of MWC 614 is not dominated by thermal emission from the dust sublimation region. However, the temperature we derived is similar to a dust sublimation temperature. As we show later, a compelling scenario to explain this particular feature could be the presence of small particles quantum heated by stellar UV photons up to the dust sublimation temperature.

MWC 614 belongs to a peculiar group of objects with regard to its CO ro-vibrational emission from fundamental lines near  $4.7 \mu\text{m}$  (mainly for the  $^{12}\text{CO}$  and  $^{13}\text{CO}$  isotopologues): van der Plas et al. (2015) and Banzatti & Pontoppidan (2015) found a single CO component emission with a high excitation temperature and estimated that it originates from a stellocentric radius of  $9.2 \pm 1.5$  au, far from the dust sublimation radius. In the group of objects presenting similar CO emission line characteristics we can find objects like HD 100546 or HD 97048 where a gap was detected (Banzatti & Pontoppidan 2015). The location of the CO emission lies just inside the inner rim that we estimated from the MIDI data set ( $12.3 \pm 0.4$  au; Section 3.2). Moreover, Banzatti & Pontoppidan (2015) argued that an efficient UV pumping mechanism is needed to explain the high excitation temperatures associated with these lines and the measured line ratio between the vibrational  $\nu = 1-0$  and  $\nu = 2-1$   $^{12}\text{CO}$  transitions. Thi et al. (2013) argued that these conditions can be met in disks with an inner hole, where gas is directly exposed to the stellar radiation (see Figure 14, right).

Another potential tracer of gaps is the PAH emission. Maaskant et al. (2014) argued that the level of PAH ionization, measured by the ratio between the PAH line at  $6.2 \mu\text{m}$  and the one at  $11.3 \mu\text{m}$ , can indicate the presence of a gap in the disk. Using the spectra by Seok & Li (2017), we computed the PAH ionization ratio  $I_{6.2}/I_{11.3}$  (which gives the ratio of the equivalent width of the 6.2 and  $11.3 \mu\text{m}$  lines) and found a value of around 3. This value is very similar to the one of Oph IRS 48, whose disk was recently found to feature an inner hole of 55 au and a PAH emission originating between 11 and

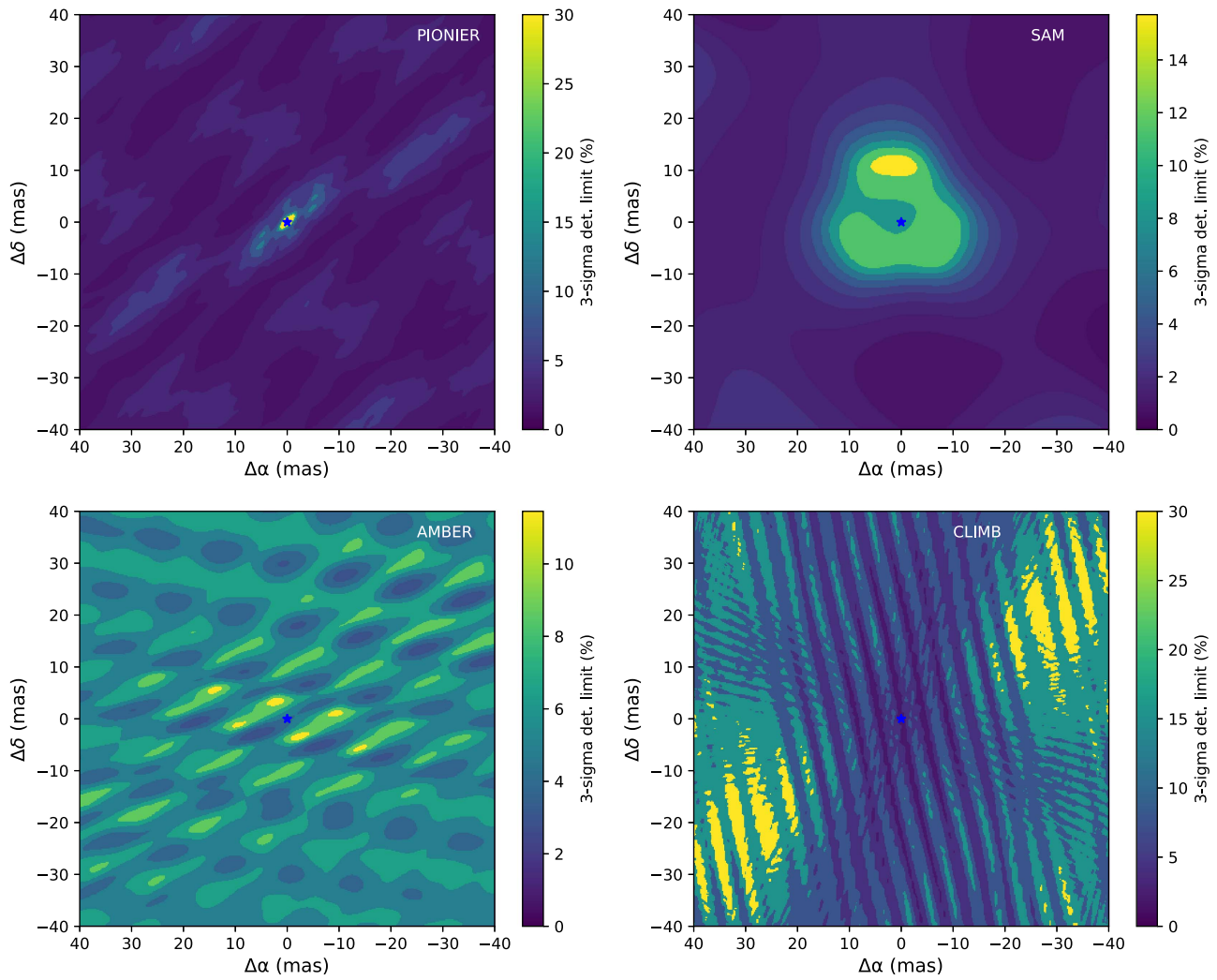


**Figure 12.** Two-dimensional maps of 3- $\sigma$  detection limits from interferometric data in the percentage of flux contribution in the respective bands. Top left: SAM; top right: PIONIER; bottom left: AMBER; bottom right: CLIMB.

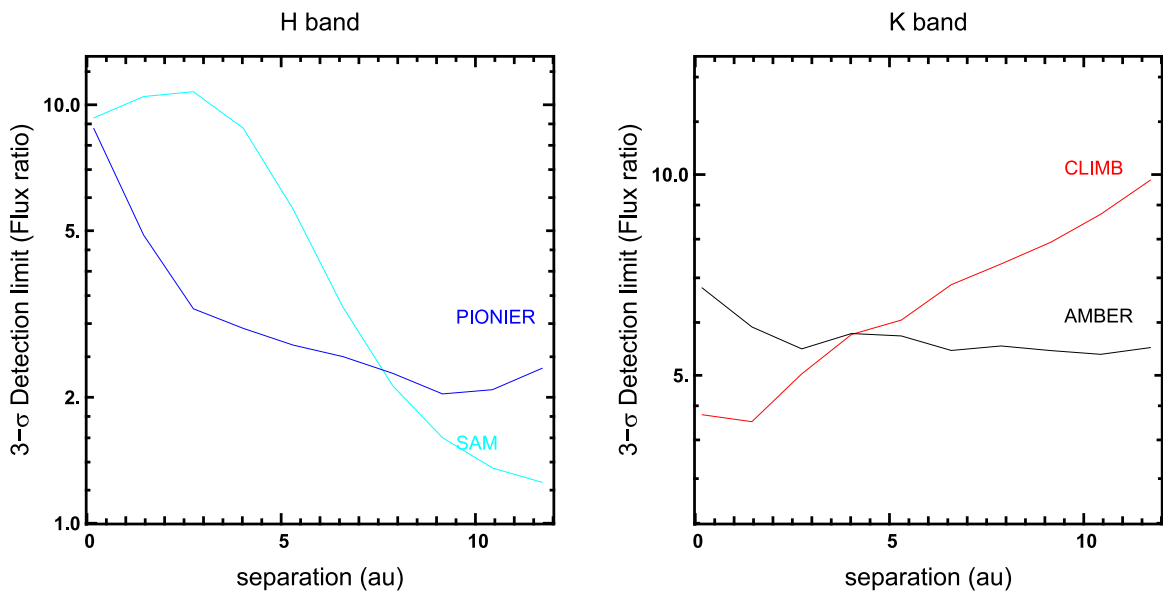


**Figure 13.** 3- $\sigma$  detection limits averaged on rings oriented in the same way as the disk. Left: *H*-band. Right: *K*-band.



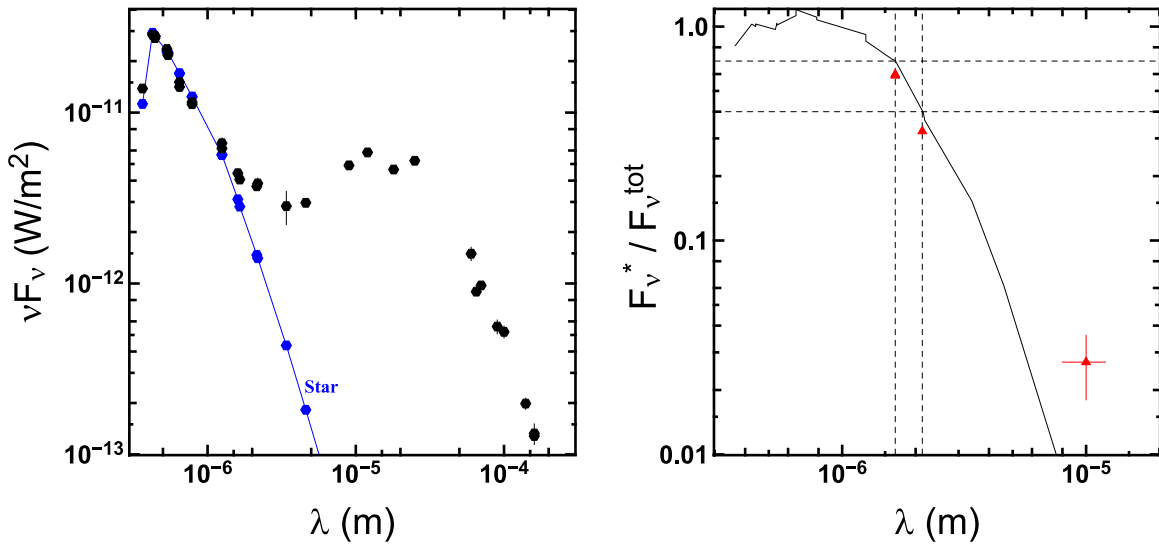


**Figure 15.** Left: SED of MWC 614 with the photometric data set (black) and the stellar photosphere (blue). Right: stellar-to-total flux ratio from the SED (black) and from the fit to the interferometric data sets (red triangles) at 1.65, 2.13, and 10  $\mu\text{m}$ .

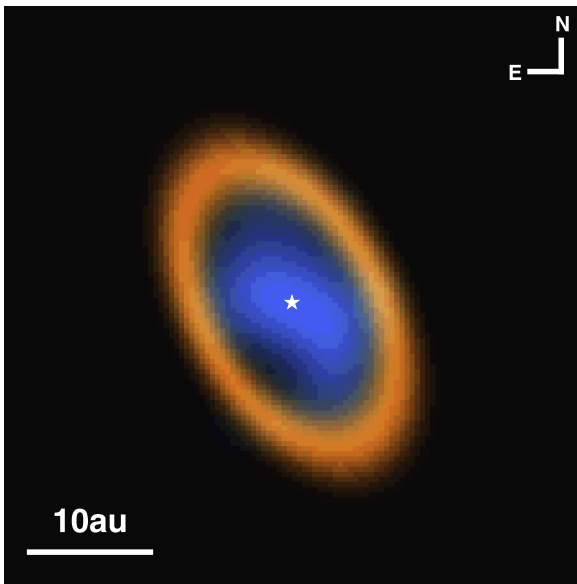


**Figure 16.** Composite image, including the best-fit MIR  $N$ -band model image (orange) and the image reconstructed from the NIR  $H$ -band data (blue). The star is indicated by the white star.

from UV-heated QHPs located in the dust cavity that was resolved with MIDI (Section 3.2). Klarmann et al. (2017) simulated the observational characteristics of QHPs in protoplanetary disks. They were able to model the overresolved disk emission associated with the transitional disk of HD 100453 by introducing QHPs inside the disk gap between 1 and 17 au. These authors also found a correlation between the amount of overresolved flux in the NIR interferometry data and the luminosity ratio between the PAHs and the UV ( $L_{\text{PAH}}/L_{\text{UV}}$ ). MWC 614 has a luminosity ratio comparable to HD 100453 ( $L_{\text{PAH}}/L_{\text{UV}} = 5.5 \times 10^{-3}$ ; Acke & van den Ancker 2004), but we show that its extended NIR emission ratio is larger ( $f_{\text{ext}}/(1-f_*) = 100\%$  compared to 25% for HD 100453, where  $f_{\text{ext}}$  is the extended-to-total flux fraction and  $f_*$  is the stellar-to-total flux fraction). This flux fraction is inferior to 30% for all the other objects from the PIONIER interferometric large program (Lazareff et al. 2017). Therefore, MWC 614 seems to

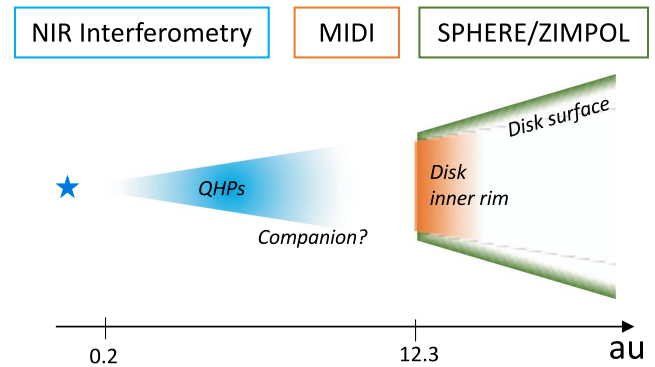


**Figure 17.** Sketch of MWC 614.

be an extreme case, where the QHP emission dominates the NIR circumstellar flux. The only object showing an extended structure in the NIR is Oph IRS 48, where the NIR flux of between 11 and 26 au was also interpreted as emission from VSGs or PAHs.

However, for Oph IRS48, the temperatures reached by the VSGs are of the order of a few hundreds of Kelvin (between 250 and 550 K; Schworer et al. 2017), far from the temperatures we derived for MWC 614. But the VSGs are located outside the first 10 au from the central star and Oph IRS48 has a luminosity of  $48 L_{\odot}$ . In the case of HD 100453, the model assumed that QHPs are distributed above the disk surface (the disk has an inner component) between 1 and 10 au with a star luminosity of  $8.04 L_{\odot}$  (Klarmann et al. 2017). The QHPs reach temperatures of between a few hundreds to 2400 K. Compared with MWC 614, where the emission is located from the star up to 8 au and with a stellar luminosity of  $100 L_{\odot}$ , we can expect even higher temperatures. The effective temperatures are therefore likely to reach the 1800 K we derived from our interferometric measurements. A full modeling of this emission is needed to confirm our scenario.

#### 4.3. Ruling Out Any Dust Material at the Dust Sublimation Radius

In Section 4.2, we estimated the theoretical location of the dust sublimation radius for MWC 614 to be 0.2 au, which

corresponds to an angular scale of around 1 mas. This should be barely resolved with the highest spatial frequencies with the VLTI baselines ( $\lambda/2B = 1.1$  mas) and well resolved with the CHARA baselines ( $\lambda/2B = 0.7$  mas). However, no clear evidence of decreasing visibility with baseline length is found.

An independent way to determine if there is still unresolved circumstellar emission in the interferometric data is to derive the stellar-to-total flux from photometric measurements and compare it with the stellar-to-total flux ratio derived from our interferometric measurements.

We used photometric measurements from the literature (see Table 6). For the photosphere effective temperature we adopted 9500 K (Montesinos et al. 2009). We then fitted the photometry in the visible with Kurucz models (Kurucz 1995). We found an  $A_V$  of 0.45 (using Cardelli et al. 1989, with  $R_V = 3.1$ ) that is comparable to previous determinations ( $A_V = 0.54$ ; van den Ancker et al. 1998). The SED and the contribution of the stellar-to-total flux ratio at each wavelength are reported in Figure 15. We found the stellar-to-total flux ratio to be  $\sim 69\%$  at  $1.65 \mu\text{m}$  and  $\sim 40\%$  at  $2.13 \mu\text{m}$ .

The stellar-to-total flux ratios derived from the NIR interferometry are lower than the ones from the SED. This is likely because the fit to the SED includes stellar light that is scattered from the disk. Given that the stellar-to-total flux ratios from the SED are higher than the ones determined from interferometric measurements, there is no evidence for the presence of an additional circumstellar component at the dust sublimation radius.

For the MIR flux, the stellar-to-total flux ratio from the SED is negligible whereas the unresolved flux from the fit to the MIDI data indicates  $2.7 \pm 0.9\%$ . However, the fit is not entirely satisfactory for the longest baselines (most sensitive to the contribution of the unresolved flux) and differs from the 0% flux ratio at a significance of  $3\text{-}\sigma$ .

Considering all these arguments, we conclude that we do not detect a significant contribution to the NIR flux from the dust sublimation region.

#### 4.4. Upper Mass Limits on a Companion Inside the Disk Cavity

The detection limits we found in Section 3.4 are defined in proportion of the flux in a given observational band. We translate these values into absolute magnitudes and onto masses using evolutionary tracks. In the  $H$ -band the detection limit varies between 1% and 3% between 2.5 and 12 au from the star, which translates into absolute magnitudes of between 4.3 and 3.2. In the  $K$ -band the detection limits are flatter and are around 5% of the  $K$ -band flux, which means an absolute magnitude of 2.0 between 0 and 12 au from the central star.

Using the evolutionary tracks of Bressan et al. (2012) (assuming a solar metallicity and an age of  $10^6$  years; Seok & Li 2017) the mass limits we derive are between  $0.14$  and  $0.34 M_\odot$  and  $0.8 M_\odot$  for the  $H$  and  $K$  bands, respectively (assuming an  $A_V$  of 0.45). Based on our data set, we can therefore rule out companions with a mass larger than  $0.34 M_\odot$  inside the cavity.

#### 4.5. Disk-clearing Mechanism

In Figure 16 we combine the best-fit model derived from our MIR interferometric data (orange) and with our NIR aperture synthesis image (blue). It is clear that the NIR flux originates

from inside the MIR-emitting ring-like disk structure at  $\sim 12.3$  au.

One mechanism that is able to open a disk gap is photo-evaporation, which happens when the disk is directly illuminated by UV or X-ray photons from the star. These disks have low accretion rates as the inner disk is not replenished by the dust from the outer parts (Owen & Clarke 2012). The accretion rate for MWC 614 has been estimated to be around  $10^{-7} M_\odot \text{yr}^{-1}$ , based on the Balmer break and the  $\text{Br}_\gamma$  line luminosity (Garcia Lopez et al. 2006; Donehew & Brittain 2011; Mendigutía et al. 2011). This high accretion rate is hardly explained by either UV or X-ray photo evaporation theories alone.

The cavity in the disk around MWC 614 might also have been opened by a low-mass companion. The presence of a reasonably sized planet ( $\sim 5 M_J$ ; Pinilla et al. 2012; Owen 2014; Zhu et al. 2014; Pinilla et al. 2016) in a disk gap can lead to dust filtering through the disk. The strong pressure gradient at the edge of a planet-opened gap can stop the inward migration of large dust grains while allowing smaller particles ( $< 1 \mu\text{m}$ , such as PAHs) to pass through (Owen 2014). As the NIR emission is likely coming from QHPs, this scenario might happen around MWC 614. The relatively high accretion rate ( $10^{-7} M_\odot \text{yr}^{-1}$ ) can replenish the cavity and a  $5 M_J$  companion could filter the dust sizes, letting small particles into the cavity. These particles are directly exposed to stellar UV light or X-rays and are quantum heated, resulting in the strong NIR emission that we detect. A quantitative validation of this scenario requires full radiative-transfer modeling, which is outside the scope of this paper.

## 5. Conclusion

Our extensive set of high angular resolution observations revealed the following properties of the surroundings of MWC 614 (see Figure 17):

1. At visual wavelengths, our SPHERE/ZIMPOL polarimetry reveals scattered light from the disk but does not resolve the inner disk cavity. The scattered light geometry is asymmetric, likely tracing the disk inclination.
2. The MIR emission ( $8\text{--}13 \mu\text{m}$ ) is confined in a ring with a radius of  $12.3 \pm 0.4$  au from the star, tracing the thermal emission of large dust grains. The ring features a relatively sharp inner edge, as indicated by the pronounced lobes that we see in the MIDI visibilities.
3. The NIR emission ( $1.2\text{--}2.5 \mu\text{m}$ ) is unusually extended (out to  $\lesssim 10$  au) and fills the region inside of the inner disk wall rather homogeneously. The emission does not trace thermal emission from material at the dust sublimation radius, as found in most other T Tauri and Herbig Ae/Be stars. Instead, the emission extends over an area that is 40 times larger, indicating that the emission traces a fundamentally different mechanism. This conclusion is also supported by the high temperature ( $1812 \pm 71$  K) that we deduce for this extended NIR component. We propose that this emission could trace a population of small QHPs that might be able to filter through the pressure bump at the inner disk wall revealed by our MIR observations. A detailed radiative transfer study will be needed to confirm this hypothesis and to develop it further.

4. Our interferometric image reveals an S-shaped asymmetry in the NIR  $H$ -band emission, indicating that the QHPs might be dynamically disturbed by a disk-clearing companion.
5. We determine an upper limit on the mass of a potential companion inside the cavity to  $0.34 M_{\odot}$  (between 2 and 12 au).

Our study indicates that the transitional disk around MWC 614 is in a very special evolutionary state, where a low-mass companion opened a gap in the disk. The inner disk could have already been accreted onto the star, exposing the PAHs of the cavity to direct stellar light. Further observations and characterization of the disk cavity (precise structure of the NIR emission, possible presence of a companion) would confirm such a scenario.

The authors acknowledge support from a Marie Skłodowska-Curie CIG grant (Grant No. 618910), Philip Leverhulme Prize (PLP-2013-110), STFC Rutherford Fellowship (ST/J004030/1), and ERC Starting Grant (Grant Agreement No. 639889). A.A. and J.D.M. acknowledge support from NSF AAG 1311698.

The authors wish to recognize and acknowledge the very significant cultural role and reverence that the summit of MaunaKea has always had within the indigenous Hawaiian community. We are most fortunate to have the opportunity to conduct observations from this mountain.

This work was supported by a NASA Keck PI Data Award, administered by the NASA Exoplanet Science Institute (PID 69/2013B\_N104N2). Data presented herein were obtained at the W. M. Keck Observatory from telescope time allocated to NASA through the agency's scientific partnership with the California Institute of Technology and the University of California. The Observatory was made possible by the generous financial support of the W. M. Keck Foundation.

This work is based in part upon observations obtained with the Georgia State University (GSU) Center for High Angular Resolution Astronomy Array at Mount Wilson Observatory. The CHARA Array is supported by the NSF under Grant No. AST-1211929. Institutional support has been provided from the GSU College of Arts and Sciences and the GSU Office of the Vice President for Research and Economic Development.

This research has made use of the SIMBAD database and the VizieR catalog access tool, operated at CDS, Strasbourg, France.

*Facilities:* VLT/SPHERE, VLTI/PIONIER, VLTI/AMBER, VLTI/MIDI, Keck:II/NIRC2, CHARA/CLASSIC, CHARA/CLIMB.

## Appendix

### A.1. Visibility Normalization

The SAM data show a relative drop in visibility, but their absolute value is difficult to calibrate. Having the VLTI/PIONIER data set in hand we calibrated the SAM data to the long-baseline interferometric data by minimizing the  $\chi^2$  with model fitting in order to account for the differences in spectral channels and the orientation of the observed object. This method assumes that there is continuity between the  $V^2$  from aperture-masking measurements and long-baseline interferometry.

Because the visibility curve does not show any Bessel lobes with spatial frequency, we used a simple model of a star and an oriented Gaussian with five free parameters: the stellar-to-total flux ratio ( $f$ ), the FWHM size of the Gaussian ( $w$ ), its inclination ( $i$ ), and its position angle ( $\theta$ ). The star can be shifted with respect to the Gaussian using two parameters ( $x_s$  and  $y_s$ ). The NIRC2 data were recorded with an  $H$  broadband filter while the PIONIER data were spectrally dispersed, covering the  $H$ -band with three channels. Therefore, we needed to parametrize the spectral dependence between the PIONIER channels in our model, which we implemented by associating the circumstellar Gaussian component with a temperature  $T$ . A complete description of the model can be found in Appendix A.3 below (here  $x_s$  and  $y_s$  equal 0). We performed the model fitting on the squared visibilities only.

In the rest of the paper we use the renormalized aperture-masking visibilities.

### A.2. Geometric Model to Fit the SPHERE Image

Here we describe the models used in Section 3.1. To build them we used one general equation and then set some parameters to 0 to obtain the desired model:

$$I_G(x, y) = \frac{f}{\sigma\sqrt{2\pi}} \exp\left(-\frac{(x'^2 + y'^2) - R}{2\sigma^2}\right) \times \left[1 + s \sin\left(\arctan\frac{y'}{x'}\right)\right], \quad (8)$$

where  $f$  is the flux in arbitrary units,  $R$  is the radius of the ring,  $s$  is the ring modulation amplitude (between  $-1$  and  $1$ ),  $\sigma = \frac{w}{2\sqrt{2\log 2}}$  with  $w$  being the FWHM, and  $x'$  and  $y'$  defined as

$$x'' = x - x_*, \quad (9)$$

$$y'' = y - y_*, \quad (10)$$

$$x' = x'' \cos \theta + y'' \sin \theta, \quad (11)$$

and

$$y' = (y'' \cos \theta - x'' \sin \theta) / \cos i, \quad (12)$$

with  $x_*$  and  $y_*$  being the coordinates of the center of the Gaussian,  $\theta$  being the position angle of the Gaussian, and  $i$  being the inclination with respect to the line of sight.

The Gaussian is centered when  $R$ ,  $x_*$ ,  $y_*$ , and  $s$  are set to 0, and the Gaussian is off center when  $R$  and  $s$  are set to 0. We obtain a Gaussian ring when  $x_*$  and  $y_*$  are set to 0.

### A.3. Geometric Model Used in Interferometric Data Modeling

The model is described with two components: the disk, which is an inclined Gaussian, and a star, which is a point source. The inclined Gaussian is geometrically described by its FWHM ( $w$ ), its inclination ( $i$ ), and its position angle ( $\theta$ ) as follows:

$$V^g(\nu') = \exp\left(-\frac{(\pi w \nu')^2}{4 \log 2}\right), \quad (13)$$

where  $V^g(\nu')$  is the visibility of the Gaussian and  $\nu' = \sqrt{u'^2 + v'^2}$  are the spatial frequencies from the  $\{u, v\}$  points oriented with respect to the object such as

$$u' = u \cos \theta + v \sin \theta \quad (14)$$

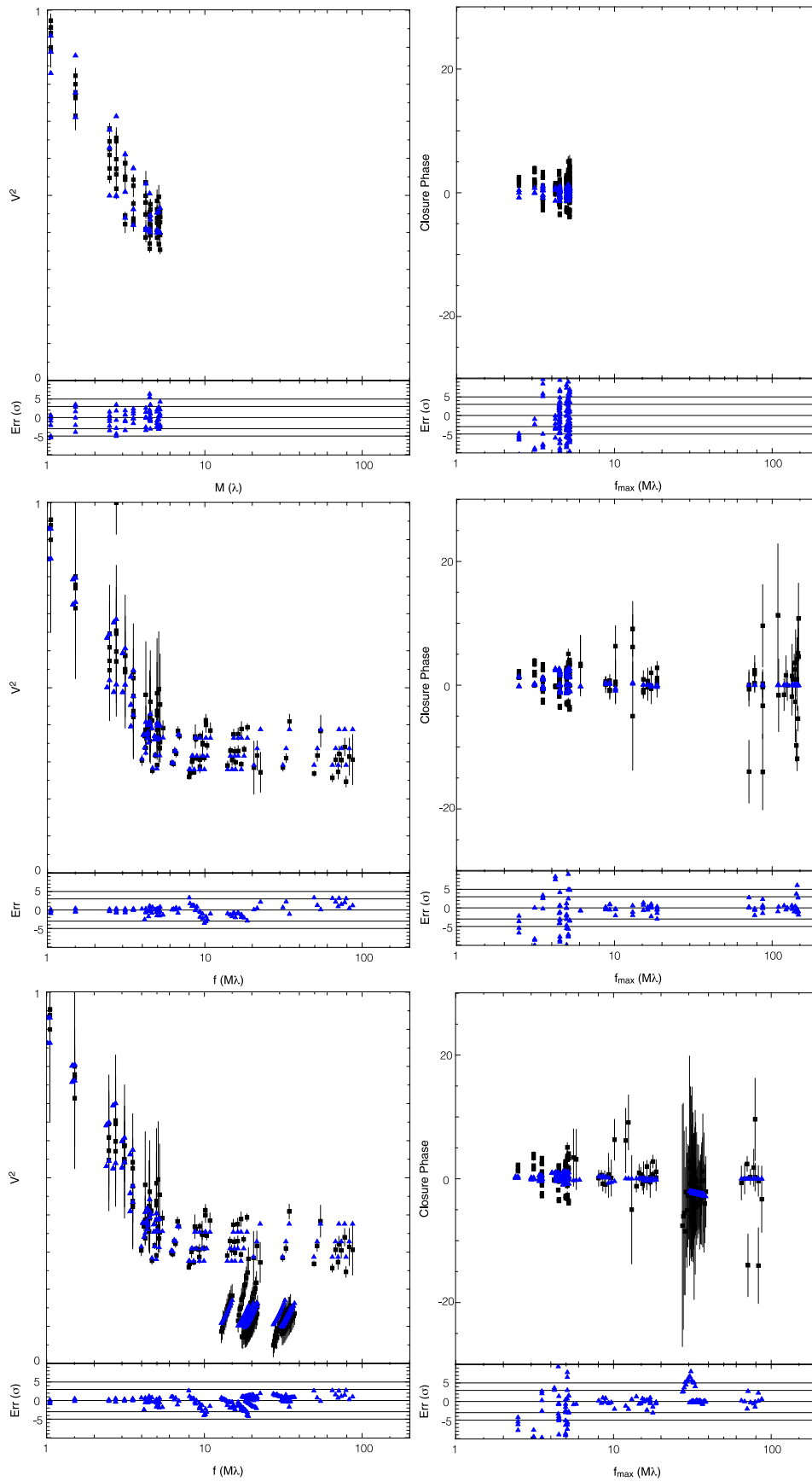


**Figure 18.** Best-fit models to the SAM (top), SAM+PIONIER (middle), and SAM+PIONIER+AMBER (bottom) data sets. Left: the fit to the  $V^2$ . Right: the fit to the CPs. The data set is in black squares and the model is the blue triangles. Below each plot is the plot of the residuals.

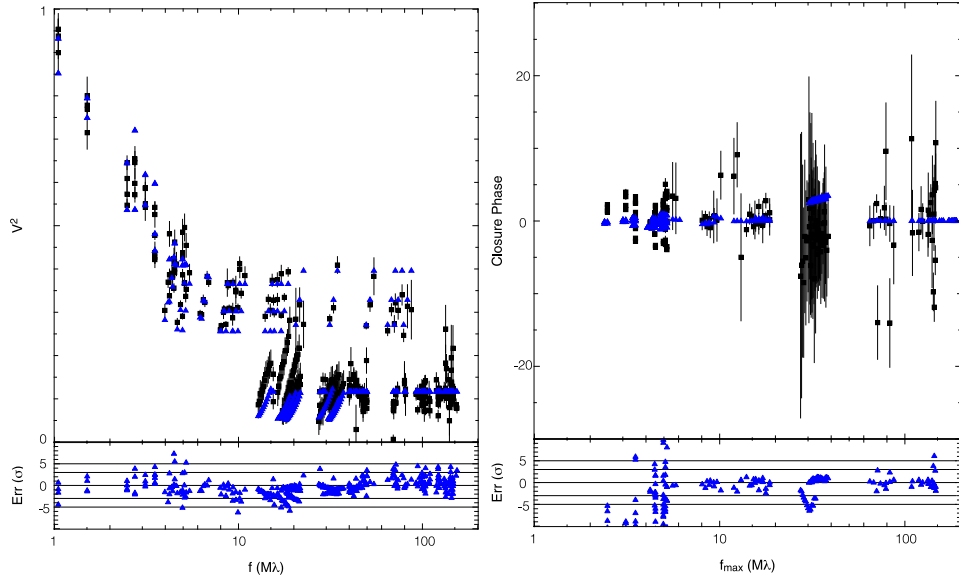


**Figure 19.** Best-fit models to the SAM+PIONIER+AMBER+CHARA data set. Left: the fit to the  $V^2$ . Right: fit to the CPs. The data set is in black squares and the model is the blue triangles. Below each plot is the plot of the residuals.

and

$$v' = (-u \sin \theta + v \cos \theta) \cos i, \quad (15)$$

with  $\nu = \sqrt{u^2 + v^2}$  as the spatial frequencies from the  $\{u, v\}$ .

The star is unresolved and can be shifted w.r.t. the center of the Gaussian by  $x_*$  and  $y_*$ :

$$V^s(\nu'') = \exp(-2i\pi\nu''), \quad (16)$$

where  $V^s(\nu'')$  is the visibility of the star and  $\nu'' = u'' + v''$  are the spatial frequencies from the  $\{u, v\}$  points shifted with respect to the Gaussian such as

$$u'' = ux_* \quad (17)$$

and

$$v'' = vy_*. \quad (18)$$

Therefore, the total visibilities are

$$V^{\text{tot}}(\nu, \lambda) = \frac{f_\lambda^g V^g(\nu) + f_\lambda^s V^s(\nu)}{f_\lambda^g + f_\lambda^s}, \quad (19)$$

with  $f_\lambda^s$  the stellar-to-total flux ratio and  $f_\lambda^g$  the Gaussian-to-total flux ratio. To define them, we have taken a reference wavelength of  $\lambda_0 = 1.65 \mu\text{m}$  (the center of the  $H$ -band). We assume that the star ( $f_\lambda^s$ ) is in the Rayleigh–Jeans regime ( $f_\lambda^s = \text{sfr}0 \left(\frac{\lambda}{\lambda_0}\right)^{-4}$ ) and that the Gaussian ( $f_\lambda^g$ ) has its own temperature so that its flux is scaled accordingly:  $f_\lambda^g = f_0 \frac{B(\lambda, T)}{B(\lambda_0, T)}$ . At  $\lambda_0$ , the sum of the stellar flux ratio, the extended flux ratio, and the inclined Gaussian flux ratio equals unity.

#### A.4. Parametric Model Results

Figures 18 and 19 show the comparison between the interferometric data and the best-fit parametric models fitted in Section 3.3.1.

#### ORCID iDs

Jacques Kluska <https://orcid.org/0000-0002-9491-393X>  
 Stefan Kraus <https://orcid.org/0000-0001-6017-8773>  
 Claire L. Davies <https://orcid.org/0000-0001-9764-2357>  
 Tim Harries <https://orcid.org/0000-0001-8228-9503>  
 John D. Monnier <https://orcid.org/0000-0002-3380-3307>  
 Alicia Aarnio <https://orcid.org/0000-0002-1327-9659>  
 Fabien Baron <https://orcid.org/0000-0002-8376-8941>  
 Rafael Millan-Gabet <https://orcid.org/0000-0003-0447-5866>  
 Theo Ten Brummelaar <https://orcid.org/0000-0002-0114-7915>  
 Sasha Hinkley <https://orcid.org/0000-0001-8074-2562>

#### References

- Absil, O., Le Bouquin, J.-B., Berger, J.-P., et al. 2011, *A&A*, 535, A68  
 Acke, B., & van den Ancker, M. E. 2004, *A&A*, 426, 151  
 Andre, P., & Montmerle, T. 1994, *ApJ*, 420, 837  
 Andrews, S. M., Wilner, D. J., Espaillat, C., et al. 2011, *ApJ*, 732, 42  
 Avenhaus, H., Quanz, S. P., Schmid, H. M., et al. 2014, *ApJ*, 781, 87  
 Banzatti, A., & Pontoppidan, K. M. 2015, *ApJ*, 809, 167  
 Benisty, M., Tatulli, E., Ménard, F., & Swain, M. R. 2010, *A&A*, 511, A75  
 Beuzit, J.-L., Feldt, M., Dohlen, K., & Mouillet, D. 2008, *Proc. SPIE*, 7014, 701418  
 Bressan, A., Marigo, P., Girardi, L., et al. 2012, *MNRAS*, 427, 127  
 Calvet, N., D'Alessio, P., Watson, D. M., et al. 2005, *ApJL*, 630, L185  
 Canovas, H., Ménard, F., de Boer, J., et al. 2015, *A&A*, 582, L7  
 Cardelli, J. A., Clayton, G. C., & Mathis, J. S. 1989, *ApJ*, 345, 245  
 Chelli, A., Utrera, O. H., & Duvert, G. 2009, *A&A*, 502, 705  
 Crida, A., Morbidelli, A., & Masset, F. 2006, *Icar*, 181, 587  
 Cutri, R. M., Skrutskie, M. F., van Dyk, S., et al. 2003, *yCat*, 2246, 0  
 Cutri, R. M., Wright, E. L., Conrow, T., et al. 2012, *yCat*, 2311, 0  
 Donehew, B., & Brittain, S. 2011, *AJ*, 141, 46  
 Dong, R. 2015, *ApJ*, 810, 6  
 Dong, R., van der Marel, N., Hashimoto, J., et al. 2017, *ApJ*, 836, 201  
 Draine, B. T., & Li, A. 2001, *ApJ*, 551, 807  
 Dullemond, C. P., & Dominik, C. 2004, *A&A*, 417, 159  
 Espaillat, C., Muzerolle, J., Najita, J., et al. 2014, in *Protostars and Planets VI*, ed. H. Beuther et al. (Tucson, AZ: Univ. Arizona Press), 497  
 Fedele, D., van den Ancker, M. E., Acke, B., et al. 2008, *A&A*, 491, 809  
 Fusco, T., Sauvage, J.-F., Petit, C., et al. 2014, *Proc. SPIE*, 9148, 91481U  
 Garcia Lopez, R., Natta, A., Testi, L., & Habart, E. 2006, *A&A*, 459, 837  
 Høg, E., Fabricius, C., Makarov, V. V., et al. 2000, *A&A*, 355, L27

- Hollenbach, D., Johnstone, D., Lizano, S., & Shu, F. 1994, *ApJ*, 428, 654
- Ishihara, D., Onaka, T., Kataza, H., et al. 2010, *A&A*, 514, A1
- Joint IRAS Science, W. G. 1994, *yCat*, 2125, 0
- Klarmann, L., Benisty, M., Min, M., et al. 2017, *A&A*, 599, A80
- Kluska, J., Benisty, M., Soulez, F., et al. 2016, *A&A*, 591, A82
- Kluska, J., Malbet, F., Berger, J.-P., et al. 2014, *A&A*, 564, A80
- Kraus, S., Ireland, M. J., Sitko, M. L., et al. 2013, *ApJ*, 768, 80
- Kraus, S., Kreplin, A., Fukugawa, M., et al. 2017, *ApJL*, 848, L11
- Kurucz, R. L. 1995, *ApJ*, 452, 102
- Lada, C. J. 1987, in *IAU Symp. 115, Star-forming Regions*, ed. M. Peimbert & J. Jugaku (Dordrecht: D. Reidel), 1
- Lazareff, B., Berger, J.-P., Kluska, J., et al. 2017, *A&A*, 599, A85
- Le Bouquin, J.-B., Berger, J.-P., Lazareff, B., et al. 2011, *A&A*, 535, A67
- Leinert, C., Graser, U., Przygodda, F., et al. 2003, *Ap&SS*, 286, 73
- Lindgren, L., Lammers, U., Bastian, U., et al. 2016, *A&A*, 595, A4
- Maaskant, K. M., Honda, M., Waters, L. B. F. M., et al. 2013, *A&A*, 555, A64
- Maaskant, K. M., Min, M., Waters, L. B. F. M., & Tielens, A. G. G. M. 2014, *A&A*, 563, A78
- Matter, A., Labadie, L., Augereau, J. C., et al. 2016, *A&A*, 586, A11
- Meeus, G., Waters, L. B. F. M., Bouwman, J., et al. 2001, *A&A*, 365, 476
- Mendigutía, I., Calvet, N., Montesinos, B., et al. 2011, *A&A*, 535, A99
- Menu, J., van Boekel, R., Henning, T., et al. 2015, *A&A*, 581, A107
- Monnier, J. D., Berger, J.-P., Millan-Gabet, R., et al. 2006, *ApJ*, 647, 444
- Monnier, J. D., & Millan-Gabet, R. 2002, *ApJ*, 579, 694
- Monnier, J. D., Millan-Gabet, R., Billmeier, R., et al. 2005, *ApJ*, 624, 832
- Montesinos, B., Eiroa, C., Mora, A., & Merín, B. 2009, *A&A*, 495, 901
- Mulders, G. D., Paardekooper, S.-J., Panić, O., et al. 2013, *A&A*, 557, A68
- Owen, J. E. 2014, *ApJ*, 789, 59
- Owen, J. E., & Clarke, C. J. 2012, *MNRAS*, 426, L96
- Owen, J. E., Ercolano, B., & Clarke, C. J. 2011, *MNRAS*, 412, 13
- Papaloizou, J. C. B., Nelson, R. P., Kley, W., Masset, F. S., & Artymowicz, P. 2007, in *Protostars and Planets V*, ed. B. Reipurth, D. Jewitt, & K. Keil (Tucson, AZ: Univ. Arizona Press), 655
- Pascual, N., Montesinos, B., Meeus, G., et al. 2016, *A&A*, 586, A6
- Petrov, R. G., Malbet, F., Weigelt, G., et al. 2007, *A&A*, 464, 1
- Pfalzner, S., Steinhausen, M., & Menten, K. 2014, *ApJL*, 793, L34
- Pinilla, P., Birnstiel, T., Ricci, L., et al. 2012, *A&A*, 538, A114
- Pinilla, P., Flock, M., Ovelar, M. D. J., & Birnstiel, T. 2016, *A&A*, 596, A81
- Pinilla, P., Pérez, L. M., Andrews, S., et al. 2017, *ApJ*, 839, 99
- Pinilla, P., van der Marel, N., Pérez, L. M., et al. 2015, *A&A*, 584, A16
- Purcell, E. M. 1976, *ApJ*, 206, 685
- Roelfsema, R., Bazzon, A., Schmid, H. M., et al. 2014, *Proc. SPIE*, 9147, 91473W
- Schworer, G., Lacour, S., Huéamo, N., et al. 2017, *ApJ*, 842, 77
- Seok, J. Y., & Li, A. 2017, *ApJ*, 835, 291
- Sheehan, P. D., & Eisner, J. A. 2017, *ApJL*, 840, L12
- Sicilia-Aguilar, A., Hartmann, L., Calvet, N., et al. 2006, *ApJ*, 638, 897
- Tannirkulam, A., Monnier, J. D., Harries, T. J., et al. 2008, *ApJ*, 689, 513
- Tatulli, E., Millour, F., Chelli, A., et al. 2007, *A&A*, 464, 29
- ten Brummelaar, T. A., Sturmman, J., McAlister, H. A., et al. 2012, *Proc. SPIE*, 8445, 84453C
- ten Brummelaar, T. A., Sturmman, J., Ridgway, S. T., et al. 2013, *JAI*, 2, 1340004
- Thi, W. F., Kamp, I., Woitke, P., et al. 2013, *A&A*, 551, A49
- Thiébaud, E. 2008, *Proc. SPIE*, 7013, 70131I
- van den Ancker, M. E., de Winter, D., & Tjin A Dje, H. R. E. 1998, *A&A*, 330, 145
- van der Marel, N., van Dishoeck, E. F., Bruderer, S., et al. 2013, *Sci*, 340, 1199
- van der Marel, N., van Dishoeck, E. F., Bruderer, S., et al. 2016, *A&A*, 585, A58
- van der Plas, G., van den Ancker, M. E., Waters, L. B. F. M., & Dominik, C. 2015, *A&A*, 574, A75
- Vieira, S. L. A., Corradi, W. J. B., Alencar, S. H. P., et al. 2003, *AJ*, 126, 2971
- Willson, M., Kraus, S., Kluska, J., et al. 2016, *A&A*, 595, A9
- Yamamura, I., Makiuti, S., Ikeda, N., et al. 2010, *yCat*, 2298, 0
- Zhu, Z., Nelson, R. P., Dong, R., Espaillat, C., & Hartmann, L. 2012, *ApJ*, 755, 6
- Zhu, Z., Stone, J. M., Rafikov, R. R., & Bai, X.-N. 2014, *ApJ*, 785, 122